Nucleic Acids Research, 2026, **54**, gkag983
https://doi.org/10.1093/nar/gkag983
Data Resources and Analyses

Data analysis of experimentally solved nucleosome arrays reveals heterogeneous features

Stephanie Portillo-Ledesma[1,4], Zilong Li[1,4], Elijah Franowicz[1], Tamar Schlick[1,2,3,4,*]

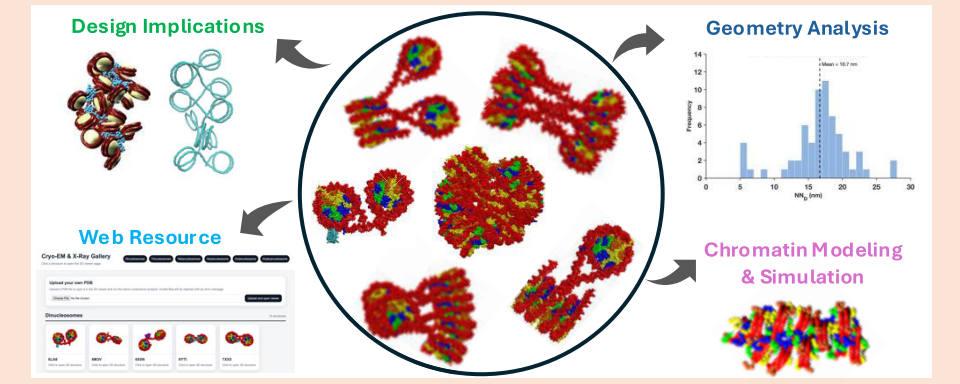
[1]Department of Chemistry, 100 Washington Square East, Silver Building, New York University, New York, NY 10003, United States
[2]Courant Institute School of Mathematics, Computing, and Data Science, New York University, 251 Mercer St., New York, NY 10012, United States
[3]New York University-East China Normal University Center for Computational Chemistry, New York University Shanghai, Shanghai 200122, China
[4]Simons Center for Computational Physical Chemistry, 24 Waverly Place, Silver Building, New York University, New York, NY 10003, United States

*To whom correspondence should be addressed. Email: schlick@nyu.edu

Abstract

Atomic-resolution nucleosome array structures have provided invaluable information on eukaryotic genome packing. Although these arrays are often obtained for regular fibers with designed sequences, such information complements *in vivo* genome organization data and modeling studies. Here, we analyze such systems with a focus on chromatin organization. We highlight both robust and unique features, as well as suitable average values for coarse-grained modeling, such as the relative orientation and positioning of neighboring nucleosomes, and opening of the linker DNA. Our associated web resource (https://www.biomath.nyu.edu/chromstruct/) shares these collected systems and provides tools for their analysis. The heterogeneous features exhibit a wide range of geometrical properties that depend on linker DNA length, core histone protein variants, auxiliary protein binding, and fiber interdigitation. Yet experimental fiber geometries can be reproduced reasonably using average parameters, as demonstrated here by simulations with our mesoscale model for regular fibers and as reported separately for life-like systems with epigenetic marks. Such analysis may also be useful for modular design of chromatin fibers. The structural characterization of these chromatin building blocks provides new insights into the regulation of chromatin architecture and has implications for the modular design of chromatin fibers.

Graphical abstract



Introduction

The eukaryotic genome is hierarchically and modularly organized to pack ∼2 meters of DNA inside the micrometer sized nucleus, thereby tightly controlling gene expression [1] (Fig. 1). At the largest scale of organization, chromosomes occupy specific regions in the nucleus where they self-interact in a non-random way, forming chromosome territories [2]. At the Mb scale, compartments A and B segregate euchromatin from heterochromatin through phase separation [3, 4]. Inside compartments, DNA organizes into topologically associated domains (TADs) that preferentially interact with each other and are actively formed by the loop extrusion mechanism directed by cohesin and CTCF [3, 5, 6].

Received: June 25, 2026. **Revised:** September 3, 2026. **Accepted:** September 17, 2026
© The Author(s) 2026. Published by Oxford University Press.
This is an Open Access article distributed under the terms of the Creative Commons Attribution-NonCommercial License (https://creativecommons.org/licenses/by-nc/4.0/), which permits non-commercial re-use, distribution, and reproduction in any medium, provided the original work is properly cited. For commercial re-use, please contact reprints@oup.com for reprints and translation rights for reprints. All other permissions can be obtained through our RightsLink service via the Permissions link on the article page on our site-for further information please contact journals.permissions@oup.com.

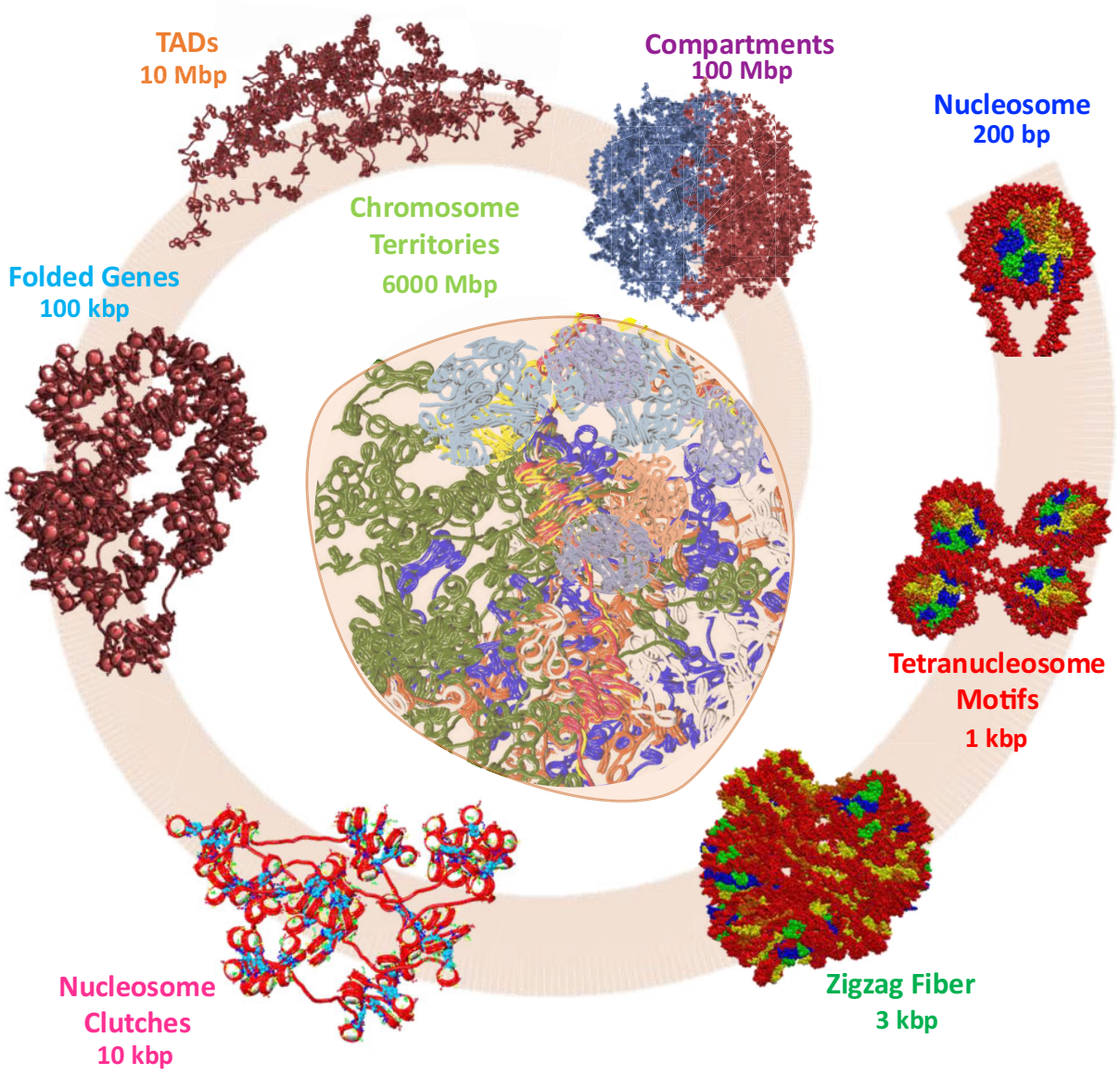


Figure 1. DNA hierarchical folding. Wrapping of DNA around the octamer of core histone proteins to form the nucleosome as the first level of organization. A few nucleosomes can organize in tetranucleosome motifs and zigzag fibers. At the nm scale, or a few kbp, nucleosomes group to create clutches of different sizes and compaction. At a larger scale, or a few hundred kb, genes fold through hierarchical looping. At the Mbp level, TADs and compartments separate active from inactive genes. Finally, chromosomes separate into discrete territories. Figure adapted from [7].

Although at a large scale chromatin organization appears irregular and dynamic [8, 9], on the small nucleosome or sub-kb level, many structural features have also been discovered by experiments and modeling. For example, nucleosomes assemble to form "clutches" [10], whose size and compaction are regulated by the cell developmental stage [11] and epigenetic marks [12]. Interesting features on the sub-nucleosome level have also been suggested. For example, tetranucleosome [13] and trinucleosome conformations [14]. Clearly, chromatin organization begins at the level of small modular units.

The growing increase in resolution reached by Cryo-EM and X-ray crystallography techniques has allowed researchers to obtain structural information of chromatin arrays at unprecedented levels. Arrays of up to 12 nucleosomes with different linker DNA lengths, auxiliary proteins, and core histone protein variants are now available [15], providing a wealth of information for detailed structural insight.

Physics-based models of chromatin fibers at nucleosome resolution use structural information from experiments to derive model parameters [16–19]. For example, the radius and width of wound DNA supercoil (r_0 and ω_0), and the angle between the entering and exiting points for linker DNA in the nucleosome (θ_0) are defined based on nucleosome crystal structures [20, 21]. Similarly, the DNA on the surface of the nucleosome core can be parametrized based on the bp parameters of nucleosome crystal structures [17]. The inclination angle defining nucleosome rotation around the dyad axis, can be defined based on electric dichroism experiments [22]. The entry–exit DNA geometry has also been parametrized using the crystal structure of a tetranucleosome array [23].

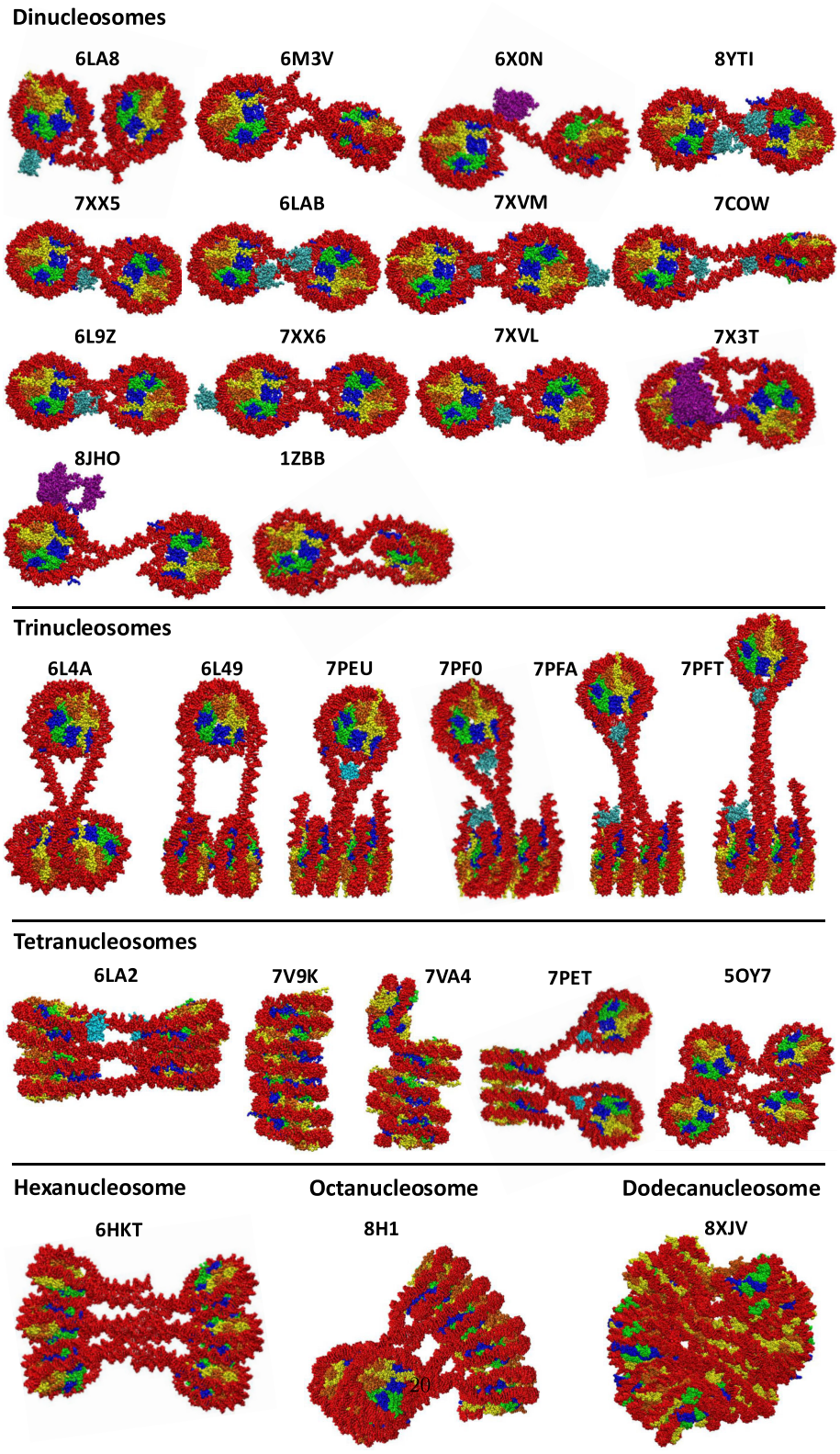


Figure 2. Nucleosome arrays studied in this work. We analyze structural properties of nucleosome arrays containing 2–12 nucleosomes solved experimentally. Histone core proteins are represented in blue (H3), green (H4), yellow (H2A), and orange (H2B), DNA in red, LHs in cyan, and other bound auxiliary proteins are shown in purple. For each structure, we specify the PDB code, except for the octanucleosome, in which case we use a code to name it.

Crystal structures of nucleosome core particles have been reviewed [24] and recently analyzed [25]. Depending on their composition, nucleosomes display a heterogeneous range of geometric features. Different ways of DNA unwinding and modes of DNA supercoiling are also observed. Experimental structures of stacked nucleosomes without linker DNA connections [26] revealed that a head-to-tail orientation and a shift of 36–44 Å are common features of nucleosome stacking. A recent database of nucleosomes and polynucleosomes also allows analysis of the relative twist and local geometry of DNA, core histone protein geometry, and DNA–protein contacts [25].

Although these *in vitro* structures do not represent *in vivo* conditions due to the regularity of the fibers combined with designed DNA sequences and absence of epigenetic factors, they form valuable references for analysis of in vivo studies and provide robust averages for modeling chromatin systems composed of repeating units. Thus, computational modeling of life-like chromatin arrays with parameters derived from these reference models remains essential for providing detailed biophysical mechanisms underlying chromatin architecture and regulation, just like simulating biomolecules relies on force fields derived from small model systems of protein and nucleic acid constituents.

Table 1. Nucleosome arrays analyzed in this work. Dinucleosomes are represented with circles; trinucleosomes with triangles; tetranucleosomes with squares; hexanucleosomes with hexagrams; octanucleosomes with stars, dodecanucleosomes with diamonds; and engineered arrays with side triangles

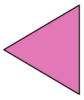
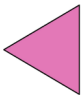
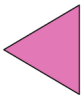
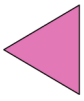
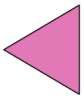
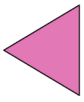
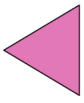
Array size (# nucleosomes)	PDB code and Ref.	Symbol in plots	DNA linker length (bp)	Auxiliary protein bound	Histone core proteins & DNA seq.
2	6LA8 [27]		29	H1.0 (Human)	Human & non-palindromic 349 bp
	6M3V [27]		31	—	Human & non-palindromic 349 bp
	6X0N [28]		20	PARP2/HPF1 (Human)	Xenopus laevis & 601 Widom
	8YTI		22	H1x (Human)	Human & Sticky 169 bp
	7XX5		22	H1.3 (Human)	Human & Sticky 169 bp
	6LAB [29]		22	H1.0 (Human)	Human & 169 bp with cohesive termini
	7XVM		22	H5 (Gallus gallus)	Human & Sticky 169 bp
	7COW [29]		31	H1.0 (Human)	Human & 353 bp with cohesive DNA termini
	6L9Z [29]		24	H1x (Human)	Human & non-palindromic 338 bp
	7XX6		22	H1.0 (Human)	Human & Sticky 169 bp
	7XVL		22	H1.0 (Human)	Human & Sticky 169 bp
	7X3T [30]		20	ISW1a (Saccharomyces cerevisiae)	Xenopus laevis & Widom 601

Table 1. Continued

Array size (# nucleosomes)	PDB code and Ref.	Symbol in plots	DNA linker length (bp)	Auxiliary protein bound	Histone core proteins & DNA seq.
	8JHO [31]		30	Rpd3S (Saccharomyces cerevisiae)	Xenopus laevis & Widom 601
	1ZBB [32]		20	—	Xenopus laevis & Widom 601
3	6L4A [33]		22	—	Human & Widom 601
	6L49 [33]		22	—	Human & Widom 601
	7PEU [34]		30	H1.4 (Human)	Human & Widom 601
	7PF0 [34]		40	H1.4 (Human)	Human & Widom 601
	7PFA [34]		50	H1.4 (Human)	Human & Widom 601
	7PFT [34]		60	H1.4 (Human)	Human & Widom 601
4	6LA2 [29]		24/29	H1.0 (Human)	Human & 343 bp with cohesive DNA termini
	7V9K [35]		0	—	Human & 151 bp human telomeric
	7VA4 [35]		0	—	Human & 151 bp human telomeric
	7PET [34]		30	H1.4 (Human)	Human & Widom 601
	5OY7 [36]		11	—	Xenopus laevis & Widom 601
6	6HKT [37]		40	H1.0b (Xenopus laevis)	Xenopus laevis & Widom 601
8	8H1* [38, 39]		30	H1.4 (Human)	Xenopus laevis & Widom 601
12	8XJV [15]		30	H5 (Gallus gallus)	Xenopus laevis & Widom 601

* 8H1 is not a PDB code but the name that we assign to the octanucleosome structure.

As far as we know, a comprehensive analysis of atomic-level chromatin units has not yet been reported. Here, we evaluate structural properties of experimentally solved nucleosome arrays of size 2 to 12 nucleosomes (Fig. 2 and Table 1) to gain insight into chromatin organization extending to the kb level. In particular, we seek to identify unique and robust features that are useful for molecular design, nanotechnology applications, and coarse grained modeling.

The paper is organized as follows:

- Analysis of geometrical properties that define the nucleosome stacking in the zigzag fiber, the relative orientation of nucleosomes, and the linker DNA path on experimental nucleosome arrays. Our associated web resource (https://www.biomath.nyu.edu/chromstruct/) collects these structural models and provides tools for their quantitative analysis.
- Modeling 16-nucleosome arrays using our mesoscale chromatin model developed with average parameter values extracted from experiments [40–42]. We analyze geometrical and compaction parameters and compare them with the experimental atomic-resolution arrays.
- Construction and mesoscale modeling of chromatin fibers of 11–13 nucleosomes using the atomic-resolution nucleosome arrays as building blocks. The idea is to suggest nanotechnology implications.
- Perspective on the importance of chromatin heterogeneity *in vivo*. We illustrate this heterogeneity with examples showing how variations in linker DNA length and epigenetic factors drive long-range contacts, as seen in Hi-C maps, and heterogeneous looping arrangements that direct genome folding and function.

From the experimental nucleosome array analysis, we find that although geometrical properties adopt some preferred values, wide variations are found for the organization of the nucleosomes with respect to one another, and for the location of the linker DNA. These variations depend on the linker DNA length, core histone protein variants, auxiliary protein binding, and fiber interdigitation. This type of analysis on chromatin structures proves useful for defining parameters for coarse-grained chromatin models.

From the mesoscale modeling [40–42] of 16-nucleosome arrays, we find that, by using reasonable average values extracted from experiments, fibers can be successfully simulated at nucleosome resolution, especially at the 5 bp resolution; geometrical parameters approximate those of experimental arrays. Thus, despite wide variations in the structural properties of small nucleosome arrays, the overall fiber architecture can be captured by using average features.

Our construction of chromatin fibers using small nucleosome arrays as building blocks shows that dinucleosomes and one trinucleosome with long linkers can be used easily as modular units for constructing larger arrays. Routine combinations of longer modular systems, such as tri, tetra, or hexanucleosomes produce clashes of nucleosomes or linker DNA. These results have implications for DNA engineering nanotechnology.

Finally, because the above analyses are performed for uniform fibers, we discuss and illustrate how incorporating heterogeneity, as found *in vivo*, is crucial for dictating genome folding. Still, we emphasize that reference fibers are useful for identifying regulating factors and deriving parameters for coarse-grained models, as well as for understanding chromatin organization at the sub-kb level.

Materials and methods

Experimentally solved nucleosome arrays

We develop a python script and a web resource to analyze PDB [43] structures of nucleosome arrays solved experimentally at atomic resolution (Fig. 2 and Table 1). We also analyze an 8-nucleosome array solved at 11 Å resolution [38] that was converted to all-atom level in a Molecular Dynamics (MD) study [39]. Specifically, we calculate the following properties (Fig. 3A):

(1) Nucleosome–nucleosome distance, NN_D
Distances between nucleosomes i and $i+1, 2$ are calculated by determining the Euclidean distance between the centers of mass of each core defined by the Cα atoms of the core's eight histone proteins.

(2) Nucleosome stacked shift, NN_S
Nucleosome shift is calculated using the method developed by Korolev *et al.* [26]. Specifically, for pairs of i and $i+2$ nucleosomes, we project the center of mass of nucleosome $i+2$ onto the disc plane of nucleosome i, and then determine the distance between nucleosome i's center of mass and the projected point. For each nucleosome, the nucleosome plane is determined by applying singular value decomposition (SVD) to the coordinates of the nucleosomal DNA base pairs. We extract the dyad axis $\hat{\mathbf{d}}$: the first right singular vector (PC1, maximum variance), corresponding to the superhelix axis of the wrapped DNA; the disc plane normal $\hat{\mathbf{n}}$: the third right singular vector (PC3, minimum variance), perpendicular to the nucleosome disc; and the axial normal $\hat{\mathbf{a}} = \hat{\mathbf{n}} \times \hat{\mathbf{d}}$, the direction in the disc plane perpendicular to the dyad axis, defining the axial plane normal.

(3) Nucleosome stacked rise, NN_R
Nucleosome rise is calculated similarly to the nucleosome shift, here by determining the distance between the center of mass of nucleosomes $i+2$ and its projection onto the plane of nucleosome i.

(4) Nucleosome dyad–dyad angle, DD_A
The dyad of a nucleosome is determined by first computing the midpoint $\mathbf{M}$ and the unit vector $\hat{V}$ between the centroids of the two H3 core histone protein chains. $\hat{V}$ defines the normal to the H3–H3 plane anchored at $\mathbf{M}$. All nucleosomal DNA base pair midpoints whose perpendicular distance to this plane is <3 Å are retained as candidates. From these candidates, the base pair closest to the geometric center of the ordered base pair array (the expected location of SHL 0) is selected as the dyad base pair. The dyad vector is the unit vector from the histone octamer center of mass to the dyad base pair. The dyad–dyad angle is then the angle between the dyad vectors of two nucleosomes (i, $i+1$ or i, $i+2$), computed over the full range 0–180°.

(5) Nucleosome plane–plane angle, PP_A
Multiple methods have been proposed to computationally define the plane of a nucleosome [26, 34, 44, 45]. Here, similar to Korolev *et al.* [26], we apply SVD to determine the nucleosome disc plane normal $\hat{\mathbf{n}}$ as described above. The plane–plane angle is calculated

as the acute angle between the disc plane normals of two nucleosomes, $\theta = \arccos(|\hat{\mathbf{n}}_i \cdot \hat{\mathbf{n}}_j|)$, which lies in the range 0–90°.

(6) Inter-linker DNA distance, LL_D
The inter-linker DNA distance is determined by first computing the center of mass (CoM) of each linker DNA segment. The linker length is estimated from the nucleosome repeat length (NRL), calculated as the total DNA strand span divided by the number of nucleosomes, minus the 147 nucleosomal DNA base pairs. For each pair of consecutive nucleosomes, a window of this linker length is placed symmetrically around the midpoint between the two flanking nucleosomes. The mean three-dimensional position of all heavy atoms within this window, on both the forward and reverse strands, defines the linker CoM. The inter-linker distance is then the Euclidean distance between the CoMs of two consecutive linker segments (linker i and linker $i+1$).

(7) DNA entry–exit angles α and β
Here, we follow the method developed by Dombrowski *et al.* [34]. A vector is aligned along the line of best fit of the 10 base pairs of linker DNA closest to the nucleosome core edge on the entry and exit sides, oriented to point away from the nucleosome center of mass. The entry–exit α angle is found by projecting this vector onto the nucleosome disc plane ($\hat{\mathbf{n}}$ obtained from SVD) and calculating the acute angle between the projected vector and the dyad axis. The entry–exit β angle is found by projecting the vector onto the axial plane, the plane containing the dyad axis and perpendicular to the disc plane, and calculating the acute angle between the projected vector and the dyad axis.

Mesoscale modeling of chromatin fibers

To compare the structural properties of experimentally solved nucleosome arrays to chromatin fibers simulated with our nucleosome-resolution mesoscale model [40, 41] (Fig. 3B), we analyze the structure of 16-nucleosome arrays with increasing uniform linker DNA length of 15–70 bp that were determined in our previous work [42]. These structures were simulated with both of our linker DNA models, the ∼9 bp [20] and the 5 bp [42] resolution models, and with and without 1 LH per nucleosome.

Our chromatin mesoscale model treats nucleosomes as disks with 300 charges distributed on their irregular surface and calculated with the DiSCO algorithm [46, 47]. Linker DNA is treated with a combined bead and wormlike-chain model where each bead intersegment can represent ∼9 or 5 bp [20, 42, 48]. N-terminal histone tails of H3, H4, H2A, and H2B core proteins, plus the C-terminal tail of H2A, are modeled with beads composed of five residues where the charges on each bead are equal to the sum of the charges of the residues that create the bead [49, 50]. The globular head and C-terminal domain of the linker histone (LH) protein are similarly described with beads composed of five residues, but each bead charge is calculated in this case with our DiSCO algorithm [51].

The energy function of the model includes stretching, bending, and twisting terms for the linker DNA (E_S, E_B, E_T), stretching and bending terms for the core histone protein tails (E_{tS} and E_{tB}) and LHs (E_{lhS} and E_{lhB}), and electrostatic (E_C) and excluded volume (E_V) interactions among all pairs of beads:

$$E_{TOT} = E_S + E_B + E_T + E_{tS} + E_{tB} + E_{lhS} + E_{lhB} + E_C + E_V, \quad (1)$$

Table 2. Summary of parameters used in our chromatin mesoscale model

Parameter	Description	Value
θ_0	Angular separation between entry and exit linker DNA at core	108°
r_0	Radius of wound DNA supercoil	4.8 nm
$2\omega_0$	Width of wound DNA supercoil	3.6 nm
L_p	Elastic bending persistence length of DNA	50 nm
l_0	Equilibrium distance between linker DNA beads	3 nm for ∼9 bp and 1.7 nm for 5 bp resolution; $bp = l_0/rise$
h	DNA stretching rigidity	6.4 kcal/mol/nm^2
g	DNA bending rigidity	5.8 kcal/mol
s	DNA twisting rigidity	14.3 kcal/mol
ϕ_0	DNA equilibrium twist value	0, ±.209 rad (0, ± 12°)

The geometry of the fiber is defined using experimentally derived values to set our model parameters (Table 2). For example, the position where the linker DNA enters and exits the core (Fig. 3B) is defined by the geometry of the wrapped DNA (ω_0, θ_0, and r_0 in Table 2) in the nucleosome crystal structure [52]. The DNA persistence length (L_p in Table 2) is defined based on experimental measurements [53]. The equilibrium distance between linker DNA beads (l_0 in Table 2) is given based on the distance between DNA base pairs (rise) of 0.34 nm and the model resolution in bp (∼9 or 5 bp) as $bp = l_0/rise$. DNA twisting rigidity (s in Table 2) is similarly obtained from experiments [54], and DNA equilibrium twist value (ϕ_0 in Table 2) is obtained from experiments to reproduce natural variations [55].

Chromatin fibers are sampled with our tailored Monte Carlo (MC) simulation protocol [16, 56] that combines global pivot fiber moves, local nucleosome, linker DNA, and LH rotation and translation moves, and regrowth moves for the core histone protein tails [49]. Fiber configurations are accepted or rejected based on the Metropolis criterion [57]. The systems analyzed here were obtained by performing 40 million MC steps for the fibers with linker DNA of ∼9 bp resolution and 80 million MC steps for the fibers with linker DNA of 5 bp resolution, as described in detail in our previous work [42]. For each system, 50 to 100 independent trajectories were performed starting from different random seed number and a residual DNA twist value of −12°, 0°, or +12° to mimic natural variations. Here, we analyze a configurational ensemble composed of the last configuration of each trajectory. Details on energy terms and parameters can be found in the supporting information of [31].

For the 16-nucleosome chromatin fibers, we measure the distance between the centers of mass of nucleosomes i and $i+1$ or $i+2$, the angle between the planes of nucleosomes i and $i+1$, and the linker DNA entry–exit angle defined by the directions of the entry and exit linker DNAs, which are

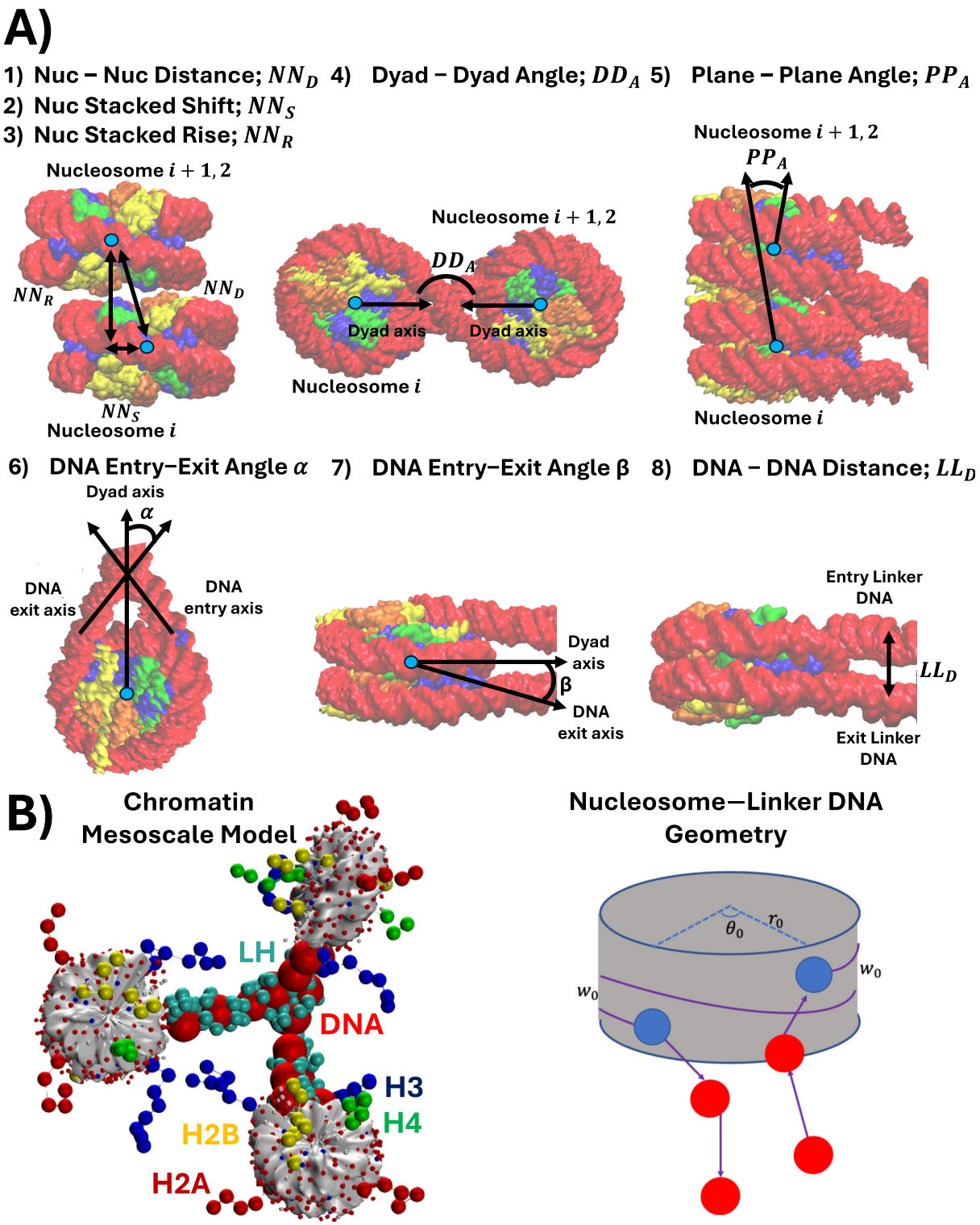


Figure 3. Structural properties calculated in this work and chromatin mesoscale model. (**A**) For experimentally determined nucleosome arrays of size 2–12 nucleosomes, we calculate the following properties: nucleosome–nucleosome distance (NN_D); stacked shift (NN_S); stacked rise (NN_R); dyad–dyad angle (DD_A); plane–plane angle (PP_A); DNA entry–exit α and β angles; and DNA–DNA distance (LL_D). The center of mass of nucleosomes is denoted with cyan circles. (**B**) Trinucleosome described with our mesoscale model showing nucleosomes with 300 charged beads; linker DNA with resolution of 5 or 9 bp; LH and core histone tails of H3, H4, H2A, and H2B with resolution of 5 residues per bead. Entering and exiting position of linker DNA (blue beads) in the nucleosome core (gray disk) on our mesoscale model depends on DNA supercoil and nucleosome size.

determined by the vector connecting the first and second DNA bead in each linker DNA.

Building candidate chromatin fibers from experimental nucleosome array structures for design applications

To generate chromatin fibers that preserve the geometric features observed in the experimental nucleosome arrays, we develop a procedure that converts the experimentally solved arrays (di, tri, tetra, hexa, octa, and dodecanucleosomes) into extended fibers through parameter extraction, helical mapping, and iterative reconstruction.

(1) Extraction of helical parameters
Crystal structures of nucleosome arrays (PDB format) are first converted into DNA-only models by retaining standard nucleic acid residues and removing all core histone protein coordinates. Helical base-pair and base-pair step parameters (Shift, Slide, Rise, Tilt, Roll, Twist) are extracted using 3DNA/DSSR [58]. This procedure generates a parameter file describing the local DNA geometry across nucleosomal and linker regions. Each nucleosome and linker segment is indexed according to residue number and stored as contiguous parameter blocks corresponding to nucleosomal cores and their connecting linker DNA.

(2) Generation of modular unit
To reproduce the spatial organization of chromatin fibers, we construct an extended parameter sequence by reusing the geometrical relationship measured between nucleosomes in the experimental crystal structure. Given an array containing N nucleosomes, each with 147 bp of DNA wrapped, we extract the experimental motif spanning nucleosome 1 to nucleosome $N-1$ (with linkers). The extracted block size in bp is then $(N-1) \times (147+L)$, where L is the linker length. Then we repeatedly append this block a user-specified number of times, generating an extended helical-parameter file that concatenates the experimentally measured nucleosome–linker relationship along the entire fiber.
For an array of N nucleosomes (e.g., di, tri, or tetranucleosome), the helical parameters are reorganized such that the terminal nucleosome of the array i is replaced by the first nucleosome of array $i+1$, thereby generating a repeating structural motif. For example:
In a dinucleosome crystal ($N=2$), the resulting helical sequence is arranged as $nuc_1 - linker_1 - nuc_1 - linker_1 \ldots - nuc_1 - linker_1 - nuc_2 - linker_2$.
In a trinucleosome crystal ($N=3$), the sequence follows: $nuc_1 - linker_1 - nuc_2 - linker_2 - nuc_1 - linker_1 - nuc_2 - linker_2 \ldots - nuc_1 - linker_1 - nuc_2 - linker_2 - nuc_3 - linker_3$.
This substitution ensures that the local nucleosome–linker geometry derived from the crystal is iteratively propagated along the fiber.

(3) Reconstruction of extended fibers
The concatenated helical parameters are then converted into three-dimensional DNA coordinates using GDash reconstruction code [59] based on the 3DNA formalism [60]. The algorithm builds the global DNA curve by propagating the transformation matrix along the chain, with each base-pair step parameter set (Shift, Slide, Rise, Tilt, Roll, Twist) sequentially converted into a local rotation matrix and translation vector. This procedure produces a one-bead-per-base-pair model, in which each bead represents the center of a base pair and is oriented according to its local helical frame. The algorithm applies the same geometric conventions as the 3DNA rebuild function, sequentially transforming base-pair step parameters (Shift, Slide, Rise, Tilt, Roll, Twist) into global Cartesian positions and orientations along the DNA path.
The resulting model contains only the DNA component—both nucleosomal and linker regions—reconstructed at base-pair resolution. This representation preserves the experimentally observed relative geometry between adjacent nucleosomes and their connecting linkers while remaining computationally lightweight for mesoscale analysis.
Following this reconstruction, nucleosomal regions (147 bp each) are identified and coarse-grained to determine nucleosome centers and orientations. The fiber is parsed in repeating blocks of: 147 bp (nucleosomal DNA) + L bp (linker) using the same linker length used for helical-parameter construction. Each nucleosome center is defined as the centroid of base-pair origins, and the nucleosome orientation ("disk normal") is obtained from the best-fit plane through these base pairs. That is, y-axis: direction from exit DNA to the center; x-axis: entry direction projected orthogonally to the y-axis; z-axis: cross product of x and y. Linker DNA is further coarse-grained using a 5-bp-per-bead representation, with bead positions assigned based on the averaged coordinates of every five consecutive base pairs. Together, these nucleosome and linker elements provided a complete mesoscale description of the chromatin fiber geometry directly derived from the experimental array structures.

(4) Monte Carlo simulations
We use our nucleosome resolution chromatin mesoscale model and perform MC simulations of 11–13-nucleosome systems constructed with the following units: 6LA8, 6M3V, and 6X0N (12-nucleosome arrays); 7PEU, 7PFT, 7PET, and 5OY7 (13-nucleosome arrays); and 6HKT (11-nucleosome array). Specifically, we run 20 million MC steps, without LH, and with a NaCl salt concentration of 150 mM. We run 10 copies for each system.

Results

As described in our web resource (https://www.biomath.nyu.edu/chromstruct/) and in Table 1 and Fig. 2, the experimental library of nucleosome arrays contains systems from 2 to 12 nucleosomes.

Fourteen different dinucleosome arrays are included. Two arrays do not have auxiliary proteins bound (1ZBB and 6M3V), nine have one or two LHs bound (7XX6, 7XVL, 7COW, 6LA8, 6L9Z, 6LAB, 7XX5, 7XVM, and 8YTI), and three of them have auxiliary proteins bound: repair protein complex PARP2–HPF1 (6X0N), chromatin remodeler complex ISW1a (7X3T), and histone deacetylase complex Rpd3S (8JHO).

Among the six trinucleosome arrays, four have LH bound and differ by the length of the linker DNA (7PEU, 7PF0, 7PFA,

and 7PFT). The other two do not contain LH and differ by the presence of CENP-A versus the canonical H3 core histone protein (6L49 and 6L4A).

Among the five tetranucleosome arrays, two have LH bound (7PET and 6LA2), two are telomeric arrays with very short linker DNA where one of the arrays is open (7VA4) and one is closed (7V9K), and one (5OY7) has short linker DNA and is arranged in an open configuration.

The hexanucleosome array (6HKT) has LHs bound, but these are not solved in the crystal structure. The octanucleosome array (8H1) and the dodecanucleosome array (8XJV) both have LH.

In Table 1, we specify the DNA sequences and origin of the recombinant core histone proteins used to construct the arrays. Most of the arrays use DNA repeats of the 601 Widom sequence and recombinant human or *Xenopus laevis* core and LHs. Some of the dinucleosomes were generated using "sticky" DNA segments that pair with each other to create the linker DNA.

Geometry between neighboring and next-neighbor nucleosomes i, $i+1$, and i, $i+2$

(1) Core–core distance, $i, i+1$
We first calculate the distance between the centers of mass of nucleosomes i and $i+1$ and between nucleosomes i and $i+2$, as described above and in Fig. 3. The $i, i+1$ distance captures local packing along the linker DNA; how tightly adjacent nucleosomes position next to each other. The $i, i+2$ distance reveals the fiber's overall geometry, distinguishing zigzag from solenoidal arrangements.
As shown in Fig. 4A, the distances between nucleosomes i and $i+1$ are in the range of 5 to 28 nm, with most of the values occurring around 17 nm. Because this distance reflects the linker DNA length, such wide variations were expected for this property as the analyzed arrays have DNA lengths that span from 0 to 60 bp (Table 1). Most of the structures have linker DNAs of 20 to 30 bp, explaining the high frequency of distances around 17 nm. This is considering that each bp in the linker DNA increases the distance between two nucleosomes by ∼0.34 nm and that the radius of the nucleosome is 5.5 nm.

(2) Core–core distance, $i, i+2$
For the distance between nucleosomes i and $i+2$ (usually stacked) (Fig. 4B), the range of values is much smaller, with most values occurring around 7 nm. There are distance outliers that correspond to the tetranucleosomes 5OY7, 7PET, 7V9K, and 7VA4.
Most of the structures have nucleosomes i and $i+2$ stacked (Fig. 2). However, in the tetranucleosome 5OY7, there is no proper stacking for the two pairs of nucleosomes i and $i+2$. This structure has a very short linker DNA, is more open, and has the nucleosome surfaces highly exposed to the solvent [36]. Similarly, in the tetranucleosome 7PET, two of the four nucleosomes are non-stacked. Such shifted and more open stacked interactions have also been observed in other array structures [38, 37]. In the arrays 7V9K and 7VA4, larger $i, i+2$ distances occur due to the stacking of all four nucleosomes in the arrays and the lack of zigzag topology.

(3) Nucleosome stacking parameters
We next calculate the shift and rise distances between nucleosomes i and $i+2$, as described above and in Fig. 3. The rise defines the vertical distance between the center of mass of a nucleosome and the plane of its stacked $i+2$ nucleosome, whereas the shift refers to the angular rotation between neighboring nucleosomes as they stack. Thus, these parameters reveal how nucleosome $i+2$ is positioned: directly stacked (high rise, low shift) or laterally shifted (high shift, low rise), which is a key characteristic for distinguishing compact zigzag/stacked fiber architectures from open or disordered ones.
The rise distances are similar to the $i, i+2$ distances, with most values around 5 nm (Fig. 4C). As outliers appear again 7V9K and 7VA4 due to the stacking of all four nucleosomes. However, no outliers are found for 7PET and 5OY7. The increase in $i, i+2$ distances seen for these tetranucleosomes is instead a product of an increase in shift (Fig. 4D).

(4) Plane–plane and dyad–dyad angles
To complete the characterization of $i, i+1, 2$ interactions, we also calculate plane–plane and dyad–dyad angles as described above and in Fig. 3. The plane–plane angle describes the way neighboring nucleosome faces orient with respect to each other and the dyad–dyad angle describes the relative orientation of the dyad axes of neighboring nucleosomes. Usually, consecutive nucleosomes $(i, i+1)$ orient in a side-to-side way, creating a plane–plane angle close to 0°. Similarly, $i, i+2$ nucleosomes that are stacking in a face-to-face way will also show values close to 0°. Thus, these geometrical parameters, sensitive to many epigenetic factors, reveal whether nucleosomes are stacked in a consistent, periodic, face-aligned way (typical of ordered zigzag/solenoid fibers) or are rotationally disordered (typical of heterogeneous, irregularly folded chromatin).
The angle between the planes of nucleosomes i and $i+2$ spans mostly from 0 to 40° (Fig. 4E). One outlier is the tetranucleosome 7VA4; one of its nucleosomes is in an open configuration and not stacked (see Fig. 2).
The plane–plane angle for $i, i+1$ interactions shows wider variations, spanning from 0 to 90°, with most of the values centered around 90° (Fig. 4E). Values close to 90° correspond to consecutive nucleosomes that orient with their faces perpendicular to each other; see for example, trinucleosomes 6L49 and 7PEU in Fig. 2.
Nucleosomes $i, i+1$ orient mostly with their dyad axis parallel, producing dyad–dyad angles between 120 and 180° (Fig. 4F). Particularly wide angles, close to 180°, correspond to the dinucleosome systems. The dinucleosome 6LA8 appears as an outlier due to the more distinctive orientation of its nucleosomes' dyad axes (Fig. 2). This array adopts an open zigzag conformation that favors fiber interdigitation instead of the typical folded helical 30 nm configuration [27].
On the other hand, nucleosomes $i, i+2$ orient their dyad axes with angles between 0 and 40° due to the stacking. Exceptions are the tetranucleosome 7V9K and 7VA4 that have much wider angles. In these structures, consecutive nucleosomes orient their dyads in

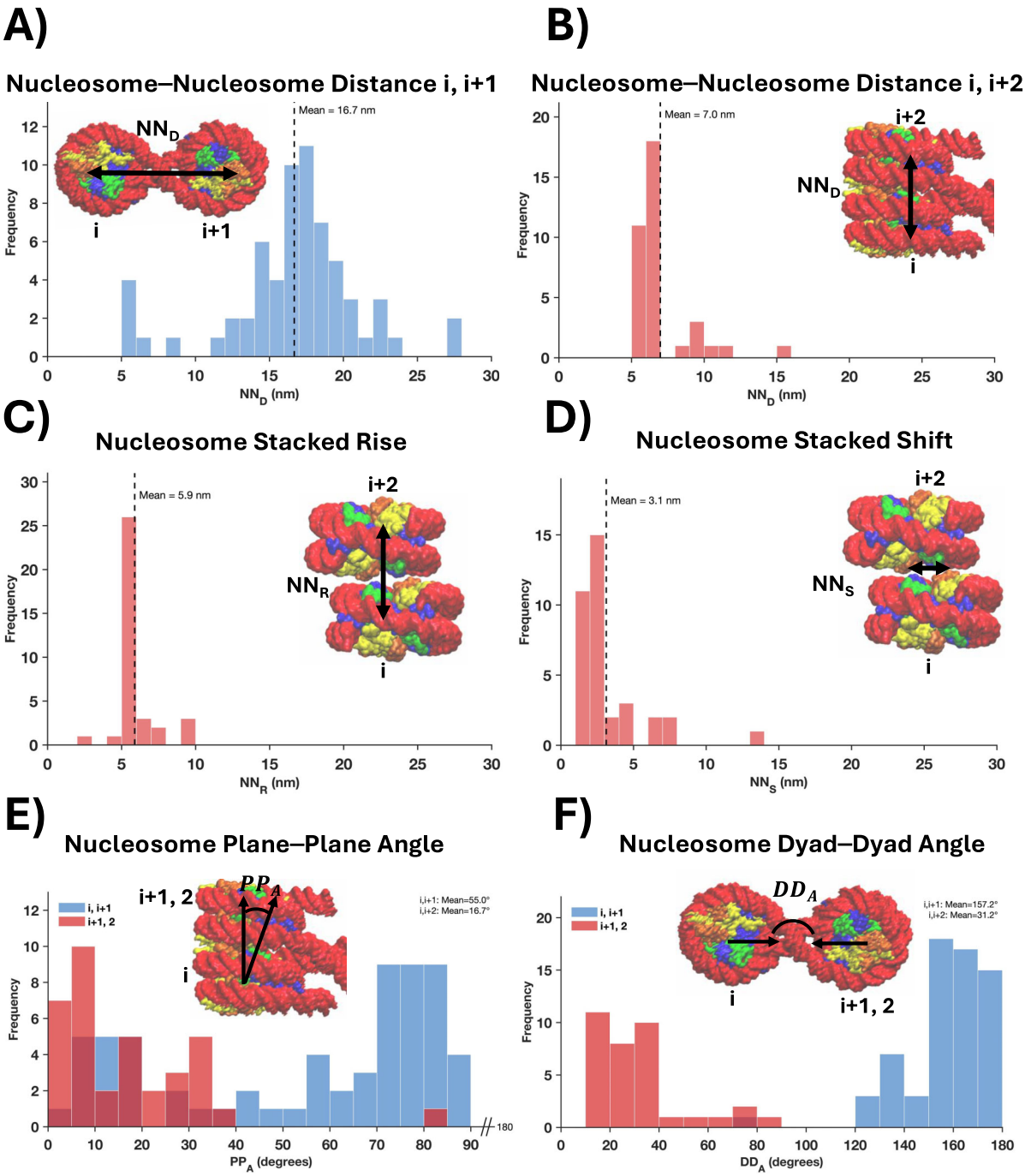


Figure 4. Positioning of nucleosome i relative to nucleosomes $i+1$ and $i+2$. Histograms for (**A**, **B**) distances between nucleosomes i and $i+1, 2$ (NN_D); (**C**, **D**) Shift and rise distances between nucleosomes i and $i+2$ (NN_S & NN_R); and (**E**, **F**) angles between the planes of nucleosomes i and $i+1, 2$ (PP_A), and between the dyads of nucleosomes i and $i+1, 2$ (DD_A).use the following standard alt text

opposite directions due to geometric restrictions created by the lack of linker DNA.

Linker DNA geometry

A major determinant of chromatin architecture is the linker DNA length, as demonstrated by modeling [61–63], *in vitro* [64, 65], and *in vivo* studies [66–69]. It can alter the relative rotational position of consecutive nucleosomes and has a profound effect on chromatin architecture, altering the accessibility to the genetic material [18, 22, 42, 70–78]. Here, we analyze the relationship between linker DNA length and the linker entry/exit α and β angles, the distance between both linkers, and the distance, dyad–dyad angle, and plane–plane angle between nucleosomes i and $i+1$.

We first examine the opening of the entry/exit linker DNAs by measuring the α and β angles as defined above and in Fig. 3. Recall that α is the angle between each linker DNA and the nucleosome plane and β is the angle between each linker DNA and the dyad axis. The α angle tends to slightly decrease with linker DNA length (Fig. 5A). This could be because longer

linkers allow higher DNA bending, whereas short linkers are more straight, as we have shown previously [61]. Similarly, the β angle also tends to decrease with linker DNA length (Fig. 5B).

As linker DNA length increases, the distance between linkers slightly decreases (Fig. 5C), and the trend follows an asymptotic behavior, with the distance converging to ∼4 nm once the linker DNA length reaches 40 bp.

An outlier appears in the trinucleosome 6L49. In this array (Fig. 2), the central nucleosome orients perpendicular to the other two nucleosomes, creating a very open linker DNA without crossing. This is due to the presence of the centromeric core histone protein H3 variant CENP-A, which creates an untwisted chromatin architecture [33]. These results highlight the epigenetic regulation of chromatin architecture by core histone protein variants.

The comparison between the trinucleosome arrays 7PEU and 6L4A (linker DNAs of 30 and 22 bp) shows the compacting effect of LH; 7PEU with LH bound has shorter linker–linker distance, and in agreement, a shorter distance and rise between the stacking nucleosomes.

Figure 5D shows, as expected, a linear relationship between the distance of nucleosomes i and $i+1$ and the linker DNA length. Fitting the data to a linear regression provides a slope of 0.28 nm/bp, close to the expected value of 0.34 nm/bp. As outlier appears the dinucleosome 6LA8 that has an open zigzag conformation and has the dyad axes oriented in a distinctive way where interdigitation is favored [27]. A more bent linker DNA results, reducing the distance between nucleosomes i and $i+1$.

Figure 5E shows the relationship between the dyad–dyad angle formed by nucleosomes i and $i+1$ versus the linker DNA length. Interestingly, we see that this property does not significantly depend on the linker DNA length. Most values are between 160° and 180°. An outlier appears again for the dinucleosome array 6LA8 due to the distinctive relative orientation of nucleosomes i and $i+1$ created by fiber interdigitation.

Wider variations are seen for plane–plane angles (Fig. 5F). These angles are distributed in two main groups: between 50° and 90° and between 0° and 20°. The structures with smaller plane–plane angles are all dinucleosomes with almost perfect side-to-side orientations, except for the trinucleosome array 6L4A. The second group contains arrays of different sizes where nucleosome faces are oriented more parallel, increasing the plane–plane angle to values closer to 90°.

Robust geometrical features of nucleosome arrays are captured by mesoscale modeling

Given these heterogeneous structural variations, the following question arises: can average values of geometric parameters be used to capture global chromatin architecture? We analyze simulations of a 16-nucleosome array with various linker DNA lengths and with and without 1 LH per nucleosome [42] in light of the experimentally determined nucleosome systems.

Our mesoscale nucleosome resolution model uses average parameter values listed in Table 2 as detailed in [50]. In particular, average parameters from elastic models of DNA are used to describe the linker DNA, but the linker DNA entering and exiting positions in the nucleosome are fixed based on the nucleosome crystal structure (see blue beads in Fig. 3B). Similarly, the initial geometries (nucleosome–nucleosome distances, rise, shift, and nucleosome–nucleosome plane angles) for ideal solenoid and zigzag fibers for the simulations are defined based on experimental structures. Thus, here we explore how well this set up captures the geometries of the experimental arrays.

Figure 6A shows the distance between nucleosomes i and $i+2$ as a function of linker DNA length for systems simulated with the ∼9 and 5 bp resolution linker DNA model, and with and without 1 LH per nucleosome. For the systems without LH, this distance increases with linker DNA length, from around 10 to 20 nm. On the other hand, the distance remains mostly constant when LH is bound due to its strong compacting effect when linker DNAs are long [61, 79]. The results obtained with both methods are consistent. When comparing these values with the experimental data reported in Fig. 4B, we see that the predicted distances from modeling are slightly larger, as most experimental structures show distances 7 nm. The experimental structures are mostly compact zigzag fibers (Fig. 2) that resemble the modeled fibers of up to∼40 bp (Fig. 6G), especially those fibers with $10n$ linkers, like the 30 bp fiber. For these modeled systems, distances between nucleosomes i and $i+2$ are around 10 nm or less, similar to the experimental values.

Next, we calculate the distance between nucleosomes i and $i+1$ as a function of linker DNA length (Fig. 6B). As expected, and similar to the trend seen for the experimental data (Fig. 5D), this distance increases linearly with linker DNA length, and the increase is slightly larger without LH. The linear fit of the data provides slopes of 0.24 and 0.22 nm/bp (black and blue lines) for the ∼9 bp resolution model without and with LH, and slopes of 0.27 and 0.26 nm/bp (red and green lines) for the 5 bp resolution model without and with LH. These results are in close agreement with the linear fit of the experimental data (Fig. 5D) that gives a slope of 0.28 nm/bp, remarkably similar to the slopes obtained with the 5 bp resolution model.

Figure 6C shows the angle between the planes of nucleosomes i and $i+1$. Similarly, both models produce consistent results, with the 9 bp model yielding larger angles. The 5 bp resolution model without LH additionally shows periodicity for short linkers of up to 35 bp with $10n$ bp linkers smaller than those for $10n+5$ bp linkers (i.e., 20 bp linkers produce smaller values than 15 and 25 bp linkers). Such periodicity was also observed in our previous work [42]. This is because the 5 bp resolution model captures the rotational setting of the nucleosomes induced by linker DNA lengths that are multiples or not of the DNA helical repeat (10 bp). This model also shows higher sensitivity to LH binding than the 9 bp model; larger differences in angle values are found and the periodicity is lost upon LH binding. When comparing with the experimental values, we see that our model produces average plane–plane angles that are slightly larger. Although wide variations are found in each fiber, the plane–plane angle is, on average, close to 100° for the ∼9 bp model and close to 50° for the 5 bp model. These differences arise because the 5 bp model better represents the rotational settings induced by the DNA helical repeat. For the experimental structures, the plane–plane angles are on average between 60° and 90° (Fig. 5F). In agreement with the experimental data, the plane–plane angle remains mostly constant as linker DNA length increases.

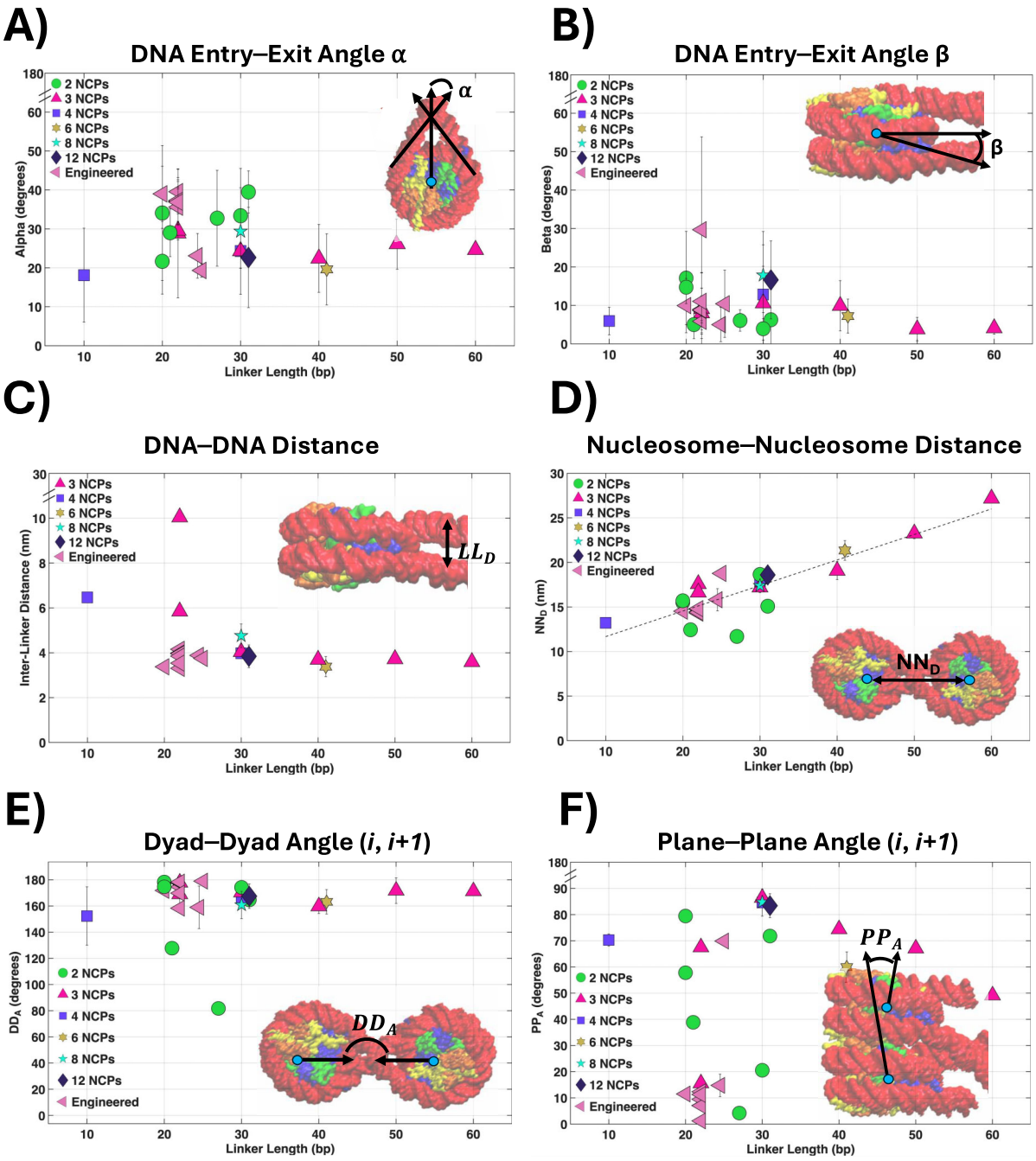


Figure 5. Linker DNA geometry and its effect on fiber architecture. Scatter plots for average and standard deviation of: (**A**, **B**) α and β linker DNA angles; (**C**) inter linker distance; (**D**) distances between cores i and $i+1$ with linear fit $y = 0.28x + 9.4$ and $R^2 = 0.81$; (**E**) dyad–dyad angle; and (**F**) plane–plane angle versus linker DNA length. For correspondence between symbol and PDB structure, see Table 1.

Figure 6D shows the relationship between the linker DNA entry-exit angle and the linker DNA length. Both the 5 bp and ∼9 bp linker DNA models produce similar values, except for the fiber with 26 bp linker DNA simulated with the ∼9 bp linker DNA model. This system shows a wide entry–exit angle of around 100°, as we have shown previously [79]. For all linker DNA lengths, the ∼9 bp model produces larger entry-exit angles that are less sensitive to the addition of LH. Both models show a slight increase in entry-exit angle with linker DNA length. This increase indicates a tighter crossing of both linkers, in agreement with the overall decrease of α and β angles seen for the experimental structures (Fig. 5A and B).

Figure 6E and F show compaction parameters like the packing ratio and sedimentation coefficient as a function of linker DNA length for both 5 and ∼9 bp linker DNA models. Similar to the PP_A plot, in both cases, a clear periodicity is seen for systems with short linkers simulated with the 5 bp model. Namely, $10n$ linkers increase compaction compared with their corresponding $10n + 5$ linkers.

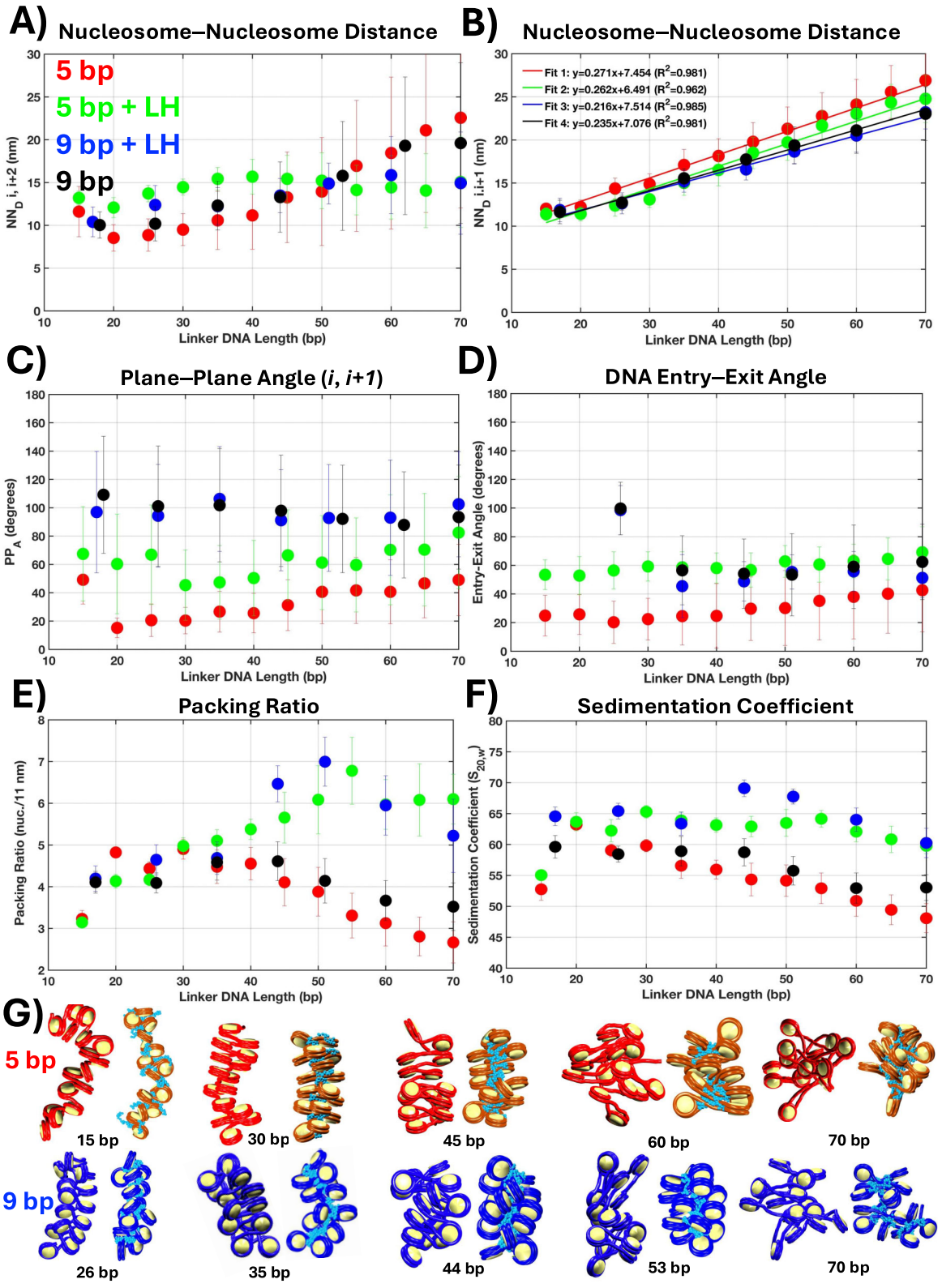


Figure 6. Fiber architecture for 16-nucleosome arrays from Mesoscale Simulations with ~9 and 5 bp linker DNA model resolution. For each fiber with different linker DNA length and with and without LH, we calculate the average and standard deviation of (**A**) distance between the centers of mass of nucleosomes i and $i + 2$; (**B**) distance between the centers of mass of nucleosomes i and $i + 1$; (**C**) plane–plane angle between nucleosomes i and $i + 1$; (**D**) linker DNA entry–exit angle; (**E**) packing ratio; and (**F**) sedimentation coefficient. (**G**) Representative fiber configurations obtained at 5 bp (red) and at ~9 bp (blue) resolution without and with LH (cyan).

As seen for the i, $i+2$ distances, the compacting effect of LH is clearly seen for both models at linker DNA lengths larger than ∼40 bp, in agreement with our previous findings [61, 79].

Overall, these results show that, although structural details might vary among different experimental nucleosome arrays, the chromatin fiber adopts an overall structure that can be captured by mesoscale models that use average parameters in the energy functions and in the description of the fiber geometry. Although average parameters resemble, in general, experimental arrays, specific parameters in coarse-grained models can be further adapted to reproduce a specific folding observed in the experimental arrays. For example, linker DNA parameters could be modified to reproduce the untwisting seen in the array containing CENP-A (6L49), similar to our modeling of the bending effect of FOXA on linker DNA [80].

Building chromatin fibers from modular units

Can these experimental data of small arrays be used to design larger chromatin fibers? Small repeating chromatin structural motifs could serve as regulators of genome function [81]. For example, dinucleosomes are the preferred substrate of chromatin regulator enzymes like HP1 and PRC [82, 83] and appear to be the basic repeating unit of tetranucleosome arrays [36]. "V"-shaped trinucleosomes have been observed in cryo-electron tomography images of human heterochromatin [14]. Similarly, tetranucleosome structural units contribute to the formation of a dodecanucleosomal 30-nm fiber [38]; they also constitute a basic secondary structural motif [13, 84] whose stability can be regulated by chromatin remodelers [85].

To explore this question, we construct nucleosome arrays of 11–13 nucleosomes by combining multiple units of dinucleosome (6LA8, 6M3V, and 6X0N), trinucleosome (7PEU and 7PFT), tetranucleosome (7PET and 5OY7), or hexanucleosome (6HKT) arrays (see Materials and methods for details and Fig. 7). Specifically, we overlap the terminal nucleosome of unit i with the first nucleosome of unit $i+1$. Although this is one way to concatenate units, other ways might be possible, for example, by overlapping only the nucleosomal DNA and not the core histones proteins or alignment of central nucleosome rather than last. The constructed arrays are then simulated with our nucleosome resolution mesoscale model and MC sampling approach.

As shown in Fig. 7, the dinucleosomes 6LA8 and 6M3V and the trinucleosome 7PFT can be used as building blocks as they produce reasonable structures for the ∼12 nucleosome chromatin arrays. While the dinucleosomes with linker DNA 27 and 31 bp produce zigzag ladder-like structures (Fig. 8), the trinucleosome 7PFT with longer linker DNA (60 bp) produces a more heterogeneous and globular structure (Fig. 8), which agrees with previous findings on the role of linker DNA length on global fiber folding [61–63].

The systems created with the dinucleosmes 6LA8 and 6M3V retain the original structure in terms of i, $i+1$ distance. However, for the 7PFT construct, the average i, $i+1$ and i, $i+2$ distances increase significantly compared to the crystal structure; around 10 nm. This results from the 60 bp linker DNA that creates a very heterogeneous folding in the construct after the MC simulation.

The other experimental arrays tested by our simple fiber building procedure produce large clashes between nucleosomes and DNA and fiber configurations are not feasible (Figs 7 and 8). These building block motifs will need to be separated by other chromatin segments to prevent steric clashes. Alternatively, topoisomerases or chromatin remodelers could help reduce steric clashes and favor a more relaxed fiber topology [86, 87].

Similar results were obtained by an MD study that constructed pentanucleosome arrays from trinucleosome units of various linker DNA lengths by superimposing nucleosome 1 of the second unit onto nucleosome 3 of the first unit [73]. There, the authors show that many structures lead to steric collisions, especially when linker DNA is short, around 20 bp. However, other structures lead to reasonable fibers. Note that the constructed pentanucleosome arrays in [73] are smaller than our ∼12 nucleosome arrays and are sampled with MD simulations, whereas we use MC sampling.

Summary and discussion

The intricate relationship between chromatin structure and function is a fascinating area of research. Many efforts have been made by experimental and modeling groups to elucidate the regulation of chromatin architecture at the kb level.

Here, we have analyzed atomic-resolution structures of nucleosome arrays solved experimentally (Fig. 2 and Table 1) and created an interactive web resource for their analysis by external users (https://www.biomath.nyu.edu/chromstruct/). We compared the experimental structures with chromatin fibers simulated with our nucleosome-resolution mesoscale model [40, 41] using average parameters, and used them as building blocks to explore the creation of larger chromatin arrays. We also analyzed these results in the context of more heterogeneous systems, as found *in vivo*.

We found that interactions between first and second neighboring nucleosomes are affected by the linker DNA length; interdigitation with another chromatin fiber; and the type of stacking interactions (i.e., type I with tight stacks between H2A–H2B dimers, or type II with offset and more open stacks [38, 37]) (Fig. 4).

In particular, short linker DNA creates an open structure in the tetranucleosome array 5OY7, but compact structures in the telomeric tetranucleosome arrays 7V9K and 7VA4 [35], similar to what is found in heterochromatin of immature retina cells [88].

The effect of fiber interdigitation has been explored by molecular modeling [89], showing that in the presence of multiple fibers, nucleosomes establish multivalent interactions instead of i, $i+2$ interactions, deviating the structure from the typical 30-nm fiber. Here we see that effect in the dinucleosome array 6LA8 where the two nucleosomes orient with a small dyad–dyad angle.

Type I and II interactions have been observed in Cryo-EM and Cryo-ET structures of reconstituted tetranucleosome arrays [38] and native chromatin fibers [90]. These structures have emphasized that native chromatin organizes with nucleosomes connected by a flexible and relaxed zigzag topology rather than straight linker DNA in a regular 30 nm fiber. The presence of epigenetic marks, auxiliary protein binding, and core histone protein variants generates deviations from average typical values.

The relationship between linker DNA and other geometrical properties has been well studied (e.g., [17, 22, 42, 61, 70,

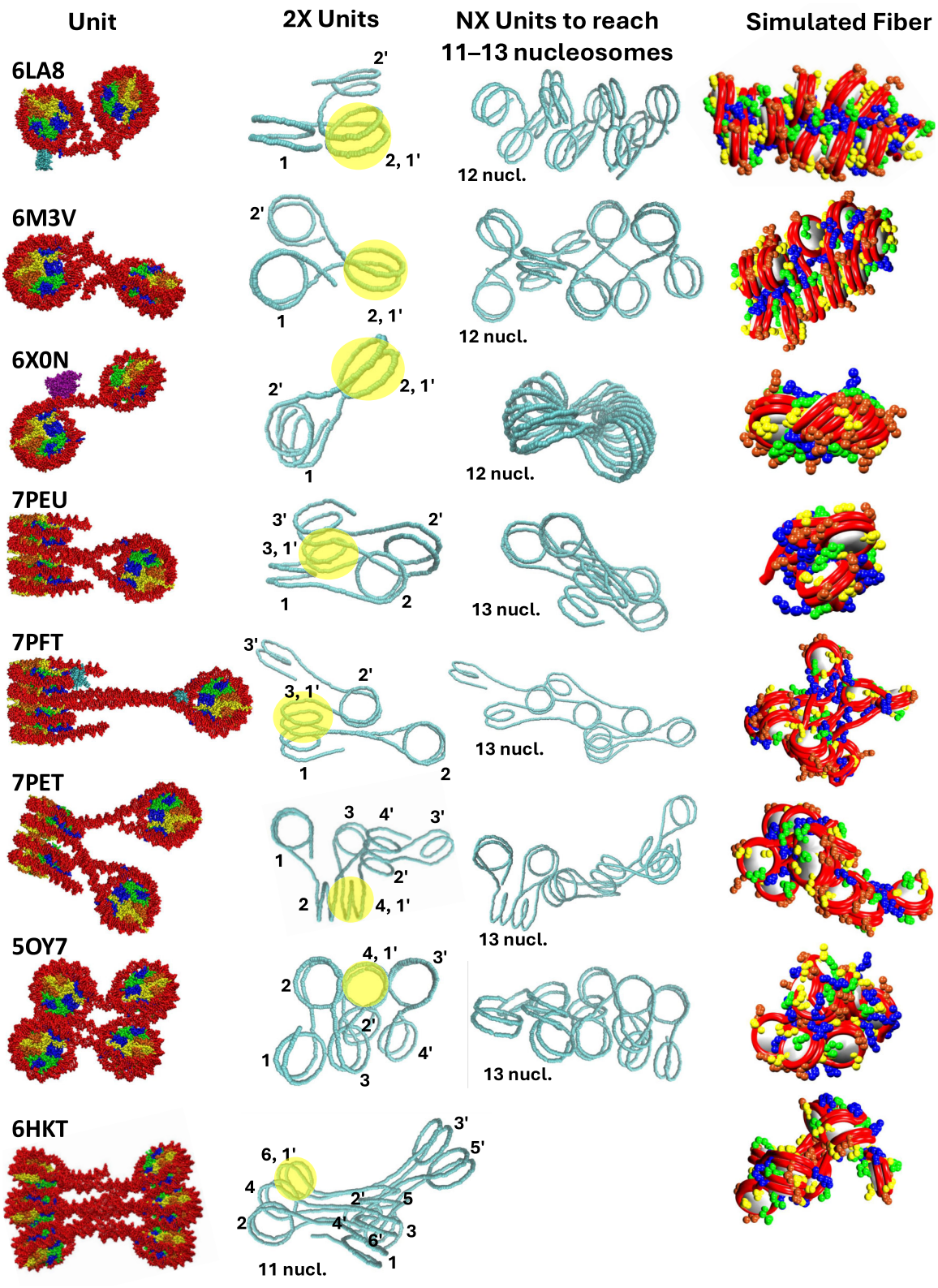


Figure 7. Construction of chromatin fibers using small nucleosome arrays as building blocks. Examples of di, tri, tetra, and hexanucleosomes used as repeating units to create larger chromatin fibers. For each system, we show from left to right: (i) the experimental structure (unit); (ii) a fiber created using two repeats of the unit where nucleosomes 1 to *N* belong to repeat 1 and 1′ to *N*′ to repeat 2, and in yellow, we highlight the overlapping of the last nucleosome of repeat 1 with the first nucleosome of repeat 2; (iii) a fiber of 11–13 nucleosomes created by using as many repeats of the unit as needed; and (iv) the 11–13-nucleosome fiber after simulated with our nucleosome resolution model with H3 tails blue, H4 tails green, H2A tails yellow, and H2B tails orange.

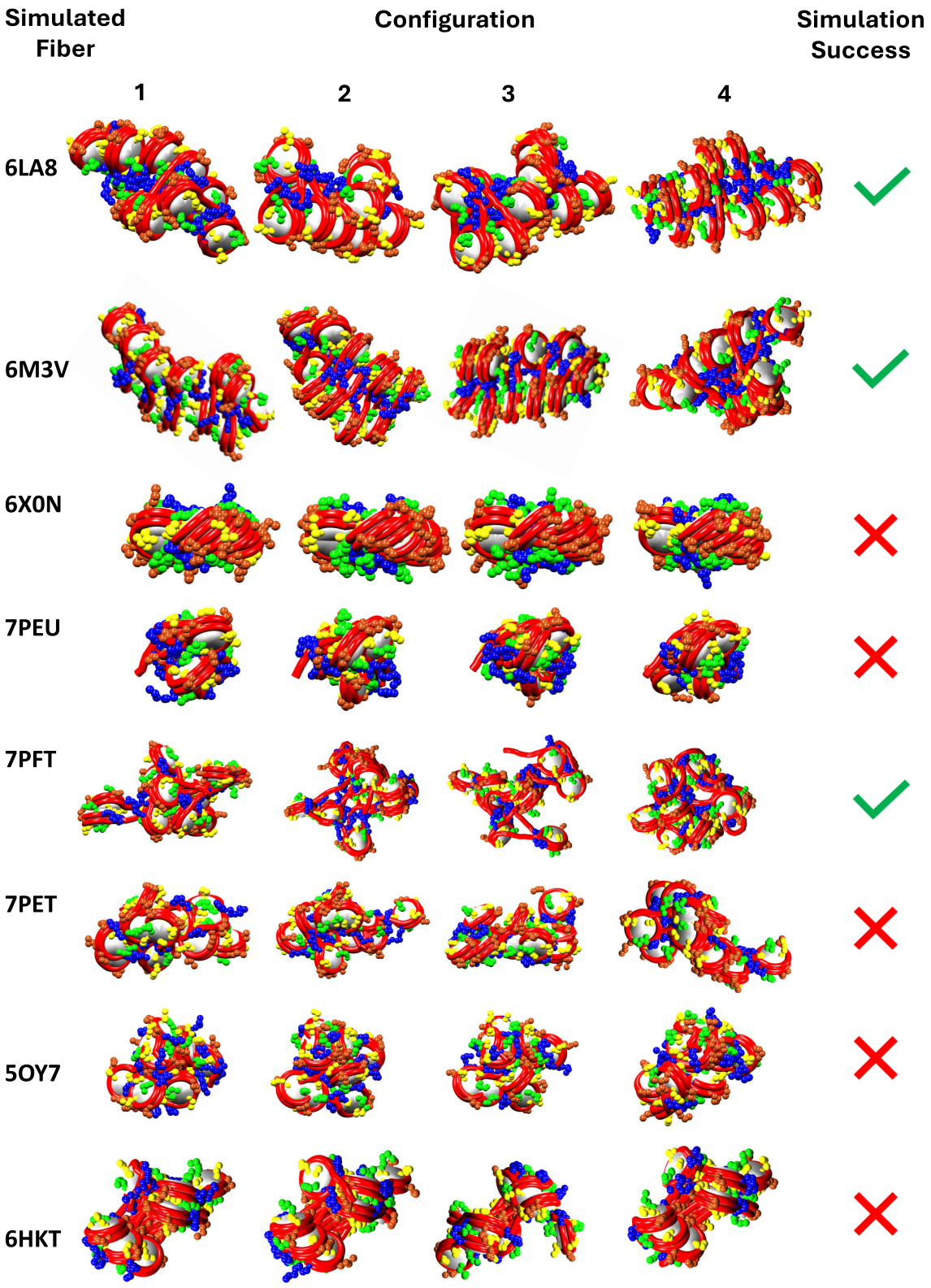


Figure 8. Configurations for fibers of 11–13 nucleosomes constructed from smaller building blocks. Four different configurations are shown for each fiber constructed from a different building block. For each system, we indicate if the simulation produced a feasible chromatin fiber or not due to steric clashes. DNA is drawn red, H3 tails blue, H4 tails green, H2A tails yellow, and H2B tails orange.

78]). Here we find that longer linkers favor the crossing of the two linker DNAs (Fig. 5), which is reflected by a small reduction of the α and β angles and the distance between linker DNAs. This agrees with previous findings showing that linker DNAs need to be long enough, around 40 bp, to allow crossover, usually induced by LH binding [15, 61, 62].

The plot of neighboring internucleosome distance versus linker DNA length (Fig. 5) shows the expected trend of increase with linker DNA length, emphasizing a shared basic folding. The structures that deviate have distinct components that make them different from the typical 30 nm fiber, such as core histone protein variants or very short linker DNAs.

The increase of plane–plane angles as linker DNA length decreases for the trinucleosome arrays 7PFT, 7PFA, 7PF0, and 7PEU has interesting implications. There is a reorientation of the central nucleosome (Fig. 2) as linker DNA length decreases, even if the DNA length is in the 10*n* bp family. Thus, changes in nucleosome rotational position are not only a product of changing the number of DNA helical repeats, but also produced by changes in linker DNA length *per se*. The longer linker reduces the stress in the DNA and in the twist energy, allowing the nucleosome to reorient [74].

Our simulated fibers of 16 nucleosomes with increasing linker DNA length (Fig. 6) show overall consistent and similar results to the experimental values. For i, $i+1$ distance versus linker DNA, the 5 bp resolution model approximates better to the experimental trend, as expected [42, 70, 74]. The best agreement with experimental data is found for fibers with short and 10*n* bp linker DNA, like the 20 or 30 bp fibers. Once linkers become longer, the fibers adopt a more heterogeneous configuration with more long range interactions [62]; these are not captured in the experimental structures due to the short size of the arrays.

The current view of chromatin organization *in vivo* highlights heterogeneity, irregularity, plasticity, and dynamics, challenging the regular 30-nm view [1, 8, 9, 91]. Although the experimentally solved nucleosome arrays studied here have uniform linkers and lack epigenetic marks, they allow us to understand how chromatin architecture is organized at a small sub-kb scale and regulated by linker DNA length, auxiliary protein binding, and core histone protein variants.

Many groups have investigated how introducing heterogeneity and *in vivo*-like factors into chromatin models affect fiber folding compared to regular fibers (see, for example, [92–96]). As we show in Fig. 9 with studies from our group, variations in linker DNA length, LH binding, and epigenetic marks are essential for shaping chromatin architecture and contributing to many genomic and biological processes such gene folding and repression, cell differentiation, and disease development.

In particular, we first showed how irregular linker DNAs, or "life-like" distributions, produce more polymorphic, flexible fibers, as well as encourage kb-range contacts via hierarchical looping, explaining the diversity of chromatin folding observed in experiments [62, 63] (Fig. 9A). Modeling LHs at various densities also revealed how its binding mode (symmetric or asymmetric), density, and dynamic binding features, as found *in vivo*, regulate fiber architecture and compaction, promote the formation of heteromorphic nucleosome clusters, and control fiber unfolding through hierarchical looping mechanism [79, 97–100]. Together these epigenetic factors (LH density, linker length, core histone tail modifications, and transcription factor binding) direct gene folding and looping in kb-range fibers [101–103]. We found that the threshold concentration of LH needed to trigger a transition into an ordered 30 nm fiber depends on the linker DNA length and that a critical value is around 0.5 LH/nucleosome [79, 101]. The interaction between tails and linker DNA also depends on both the DNA length and LH density [101]. The effect of LH on fiber folding and compaction is regulated by core histone tail acetylation; binding of LH to non acetylated regions produces hierarchical looping and segregation of acetylated from wild-type regions [102].

These findings make clear that accounting for fiber heterogeneity is essential for structural and mechanistic capturing of gene folding found *in vivo*. This includes incorporating genomic contacts, nucleosome positions, LH and transcription factor binding locations, and core histone tail acetylation and methylation locations. Using such heterogeneous settings, the folding of several genes like GATA4 [104], HOXC [105] (Fig. 9B), Pou5f1 [11], Eed [103] (Fig. 9C), and HTT [106] (Fig. 9D), as well as the X-chromosome inactivation center [107] (Fig. 9E) were successfully studied.

Our most recent study of *in vivo* chromatin used experimental Cryo-ET images to define linker DNA lengths in chromatin models of immature and mature retina cells (Fig. 9F) [88]. These simulations clearly show how heterogeneous linker DNA length is, spanning from ∼0 to 100 bp in a small kb genomic region, and how such variations regulate chromatin higher-order and dictate cell maturation. Although conversion of Cryo-ET images into 3D parameters needed for chromatin modeling requires specialized programs, such general utilities can be developed in the future. See references [108–110] for recent efforts.

Thus, overall, using a parametrized nucleosome-resolution model of polynucleosome beads on atomic-level experimental data incorporated in a heterogeneous setting can provide insights into how epigenetic factors and specific nucleosome positioning regulate many processes such as cell differentiation, gene folding, gene repression, chromosome inactivation, and heterochromatin formation. These features can be obtained for nucleosome-resolution models parametrized based on these experimental systems.

Overall, our work summarizes the most typical structural parameters adopted by small chromatin arrays (Figs 4 and 5) and how these are modulated by several factors like linker DNA length, core histone protein variants, auxiliary protein binding, and fiber interdigitation. This information serves as reference for coarse-grained modeling.

The motifs we analyzed can also be used as modular building blocks (Figs 7 and 8) for nucleic acid design, with care in assembly to ensure geometric fit and avoidance of steric incompatibilities. These ideas could be relevant for the emerging field of chromatin engineering [111] to create more compact or open chromatin segments to regulate gene expression. Artificial intelligence tools should be able to construct reliable and physically meaningful computational systems more easily. Already, promising chromatin-based therapies employ "writer" and "eraser" proteins for directing epigenetic modifications to specific genomic regions [112]; in this way, local chromatin compaction can be regulated for exciting biomolecular applications.

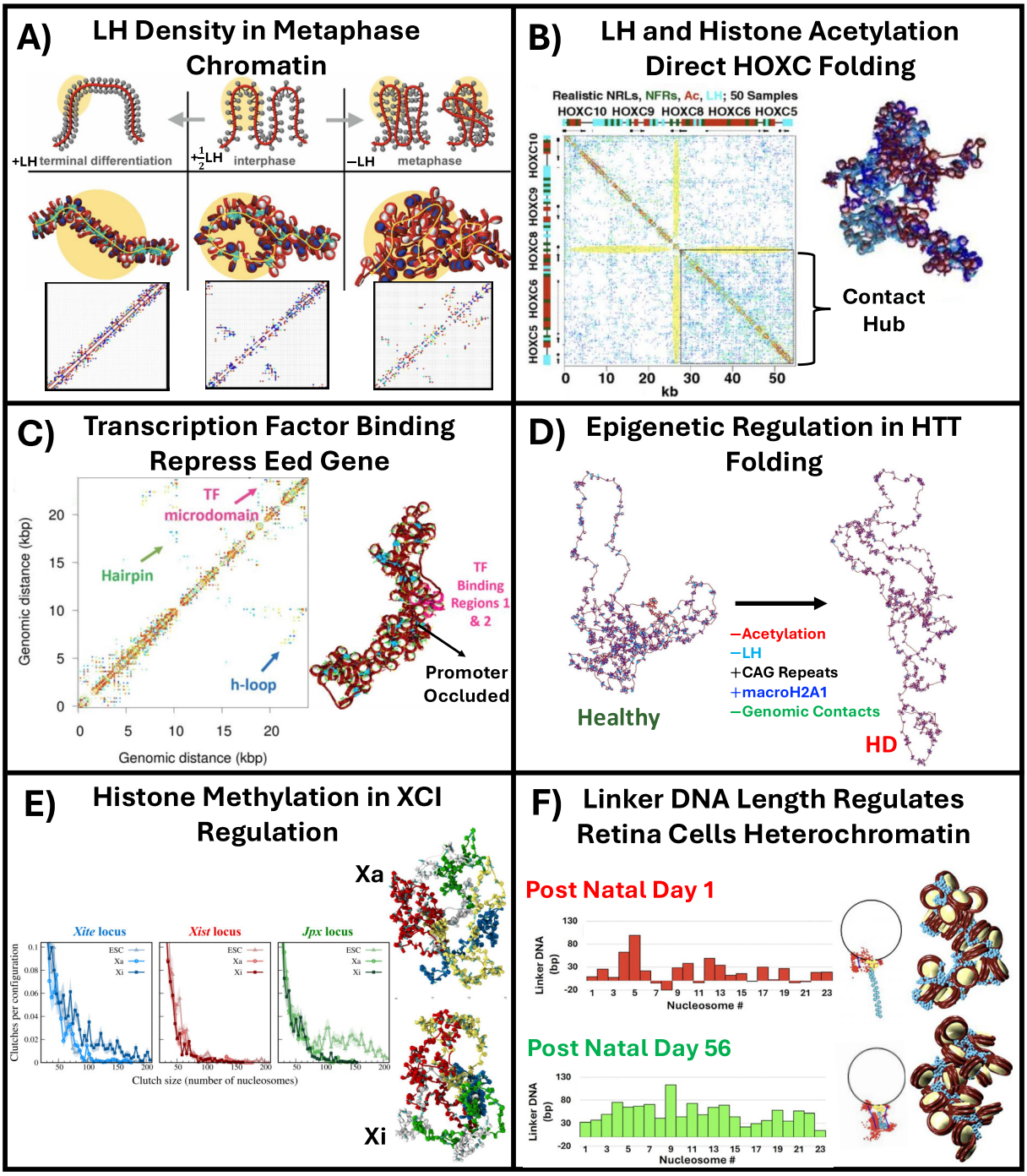


Figure 9. Effect of *in vivo* factors on chromatin folding. (**A**) Reduction of LH density associated to metaphase enables hierarchical looping folding and long-range interactions [100]. (**B**) Specific positioning of LH and core histone acetylation in the HOXC gene directs its folding to create a contact hub [105]. (**C**) Transcription factor binding to the Eed gene occludes the promoter region, suppressing gene activation [103]. (**D**) Changes in the epigenetic landscape associated with Huntington's disease trigger HTT opening, favoring disease progression [106]. (**E**) Core histone methylation marks tightly control the inactivation of the X chromosome by differentially regulating Xite, Xist, and Jpx gene loci, specifically compacting the Xite locus [107]. (**F**) The increase of linker DNA length as found experimentally during mouse retina cell maturation (post natal day 1 versus 56) allows tight binding to linker DNA by LH, triggering heterochromatin formation by DNA stem formation [88].

Acknowledgements

We thank the NYU IT High Performance Computing (HPC) group, which provided resources, services, and expert advice. We also thank Prof. Jeff Wereszczynski for kindly providing the atomic structure of the 8-nucleosome array.

Author contributions: Stephanie Portillo-Ledesma (Conceptualization [lead], Data curation [lead], Formal analysis [lead], Investigation [lead], Methodology [lead], Software [equal], Writing—original draft [lead], Writing—review & editing [lead]), Zilong Li (Data curation [equal], Formal analysis [equal], Methodology [equal], Software [lead]), Elijah Franowicz (Data Curation [equal], Formal analysis [equal], Methodology [equal], Software [equal]), and Tamar Schlick (Conceptualization [equal], Funding acquisition [lead], Investigation [equal], Project administration [equal], Supervision [equal], Writing—review & editing [equal]).

Conflict of interest

The authors declare that they have no competing interests.

Funding

This work was supported by the National Institutes of Health, National Institutes of General Medical Sciences Award R35-GM122562, the National Science Foundation Awards 2151777 and 2330628 from the Division of Mathematical Sciences and Award 2337391 from the Molecular Cellular Biosciences Core Programs, and Philip-Morris International to T.S. Support from the Simons Center for Computational Physical Chemistry at NYU to S.P.-L., Z.L., and T.S. is also acknowledged (Simons Foundation Grant No. 839534 to M.E.T.).

Data availability

The python codes for the analysis of nucleosome crystal structures and for construction of fibers from modular units are deposited on the Zenodo repository (https://zenodo.org/records/22816644). The web resource for structure analysis is available at (https://www.biomath.nyu.edu/chromstruct/). The working code for the chromatin mesoscale simulations is available at https://github.com/Schlicklab/BDiSCO.

References

1. Misteli T. The self-organizing genome: principles of genome architecture and function. *Cell* 2020;183:28–45. https://doi.org/10.1016/j.cell.2020.09.014
2. Cremer T, Cremer M. Chromosome territories. *Cold Spring Harb Perspect Biol* 2010;2:a003889.
3. Lieberman-Aiden E, van Berkum NL, Williams L *et al.* Comprehensive mapping of long-range interactions reveals folding principles of the human genome. *Science* 2009;326:289–93. https://doi.org/10.1126/science.1181369
4. Mirny LA, Imakaev M, Abdennur N. Two major mechanisms of chromosome organization. *Curr Opin Cell Biol* 2019;58:142–52. https://doi.org/10.1016/j.ceb.2019.05.001
5. Dixon JR, Selvaraj S, Yue F *et al.* Topological domains in mammalian genomes identified by analysis of chromatin interactions. *Nature* 2012;485:376–80. https://doi.org/10.1038/nature11082
6. Sexton T, Yaffe E, Kenigsberg E *et al.* Three-dimensional folding and functional organization principles of the Drosophila genome. *Cell* 2012;148:458–72. https://doi.org/10.1016/j.cell.2012.01.010
7. Portillo-Ledesma S, Li Z, Schlick T. Genome modeling: from chromatin fibers to genes. *Curr Opin Struct Biol* 2023;78:102506. https://doi.org/10.1016/j.sbi.2022.102506
8. Maeshima K, Ide S, Babokhov M. Dynamic chromatin organization without the 30-nm fiber. *Curr Opin Cell Biol* 2019;58:95–104. https://doi.org/10.1016/j.ceb.2019.02.003
9. Maeshima K. The shifting paradigm of chromatin structure: from the 30-nm chromatin fiber to liquid-like organization. *Proc Japan Acad Series B* 2025;101:339–56. https://doi.org/10.2183/pjab.101.020
10. Ricci MA, Manzo C, García-Parajo MF *et al.* Chromatin fibers are formed by heterogeneous groups of nucleosomes *in vivo* 2015;160:1145–58. https://doi.org/10.1016/j.cell.2015.01.054
11. Gómez-García PA, Portillo-Ledesma S, Neguembor MV *et al.* Mesoscale modeling and single-nucleosome tracking reveal remodeling of clutch folding and dynamics in stem cell differentiation. *Cell Rep* 2021;34:108614. https://doi.org/10.1016/j.celrep.2020.108614
12. Otterstrom J, Castells-Garcia A, Vicario C *et al.* Super-resolution microscopy reveals how histone tail acetylation affects DNA compaction within nucleosomes *in vivo*. *Nucleic Acids Res* 2019;47:8470–84. https://doi.org/10.1093/nar/gkz593
13. Ohno M, Ando T, Priest DG *et al.* Sub-nucleosomal genome structure reveals distinct nucleosome folding motifs. *Cell* 2019;176:520–34. https://doi.org/10.1016/j.cell.2018.12.014
14. Cai S, Böck D, Pilhofer M *et al.* The *in situ* structures of mono-, di-, and trinucleosomes in human heterochromatin. *Mol Biol Cell* 2018;29:2450–57. https://doi.org/10.1091/mbc.E18-05-0331
15. Li W, Hu J, Song F *et al.* Structural basis for linker histone H5–nucleosome binding and chromatin fiber compaction. *Cell Res* 2024;34:707–24. https://doi.org/10.1038/s41422-024-01009-z
16. Sun J, Zhang Q, Schlick T. Electrostatic mechanism of nucleosomal array folding revealed by computer simulation. *Proc Natl Acad Sci USA* 2005;102:8180–5. https://doi.org/10.1073/pnas.0408867102
17. Clauvelin N, Lo P, Kulaeva OI *et al.* Nucleosome positioning and composition modulate *in silico* chromatin flexibility. *J Phys Condens Mat* 2015;27:064112. https://doi.org/10.1088/0953-8984/27/6/064112
18. Zhurkin VB, Norouzi D. Topological polymorphism of nucleosome fibers and folding of chromatin. *Biophys J* 2021;120:577–85. https://doi.org/10.1016/j.bpj.2021.01.008
19. Lequieu J, Córdoba A, Moller J *et al.* 1CPN: a coarse-grained multi-scale model of chromatin. *J Chem Phys* 2019;150:215102. https://doi.org/10.1063/1.5092976
20. Beard DA, Schlick T. Computational modeling predicts the structure and dynamics of chromatin fiber. *Structure* 2001;9:105–14. https://doi.org/10.1016/S0969-2126(01)00572-X
21. Koslover EF, Fuller CJ, Straight AF *et al.* Local geometry and elasticity in compact chromatin structure. *Biophys J* 2010;99:3941–50. https://doi.org/10.1016/j.bpj.2010.10.024
22. Norouzi D, Zhurkin VB. Topological polymorphism of the two-start chromatin fiber. *Biophys J* 2015;108:2591–600. https://doi.org/10.1016/j.bpj.2015.04.015
23. Kepper N, Foethke D, Stehr R *et al.* Nucleosome geometry and internucleosomal interactions control the chromatin fiber conformation. *Biophys J* 2008;95:3692–705. https://doi.org/10.1529/biophysj.107.121079
24. Tan S, Davey CA. Nucleosome structural studies. *Curr Opin Struct Biol* 2011;21:128–36. https://doi.org/10.1016/j.sbi.2010.11.006
25. Armeev GA, Gribkova AK, Shaytan AK. NucleosomeDB—a database of 3D nucleosome structures and their complexes with comparative analysis toolkit. bioRxiv,

https://doi.org/10.1101/2023.04.17.537230, 18 April 2023, preprint: not peer reviewed.
26. Korolev N, Lyubartsev AP, Nordenskiöld L. A systematic analysis of nucleosome core particle and nucleosome–nucleosome stacking structure. *Sci Rep* 2018;8:1543. https://doi.org/10.1038/s41598-018-19875-0
27. Adhireksan Z, Sharma D, Lee PL *et al.* Near-atomic resolution structures of interdigitated nucleosome fibres. *Nature Comm* 2020;11:4747. https://doi.org/10.1038/s41467-020-18533-2
28. Bilokapic S, Suskiewicz MJ, Ahel I *et al.* Bridging of DNA breaks activates PARP2–HPF1 to modify chromatin. *Nature* 2020;585:609–13. https://doi.org/10.1038/s41586-020-2725-7
29. Adhireksan Z, Sharma D, Lee PL *et al.* Engineering nucleosomes for generating diverse chromatin assemblies. *Nucleic Acids Res* 2021;49:e52. https://doi.org/10.1093/nar/gkab070
30. Li L, Chen K, Sia Y *et al.* Structure of the ISW1a complex bound to the dinucleosome. *Nat Struct Mol Biol* 2024;31:266–74. https://doi.org/10.1038/s41594-023-01174-6
31. Li W, Cui H, Lu Z *et al.* Structure of histone deacetylase complex Rpd3S bound to nucleosome. *Nat Struct Mol Biol* 2023;30:1893–901. https://doi.org/10.1038/s41594-023-01121-5
32. Schalch T, Duda S, Sargent DF *et al.* X-ray structure of a tetranucleosome and its implications for the chromatin fibre. *Nature* 2005;436:138–41. https://doi.org/10.1038/nature03686
33. Takizawa Y, Ho C, Tachiwana H *et al.* Cryo-EM structures of centromeric tri-nucleosomes containing a central CENP-A nucleosome. *Structure* 2020;28:44–53. https://doi.org/10.1016/j.str.2019.10.016
34. Dombrowski M, Engeholm M, Dienemann C *et al.* Histone H1 binding to nucleosome arrays depends on linker DNA length and trajectory. *Nat Struct Mol Biol* 2022;29:493–501. https://doi.org/10.1038/s41594-022-00768-w
35. Soman A, Wong SY, Korolev N *et al.* Columnar structure of human telomeric chromatin. *Nature* 2022;609:1048–55. https://doi.org/10.1038/s41586-022-05236-5
36. Ekundayo B, Richmond TJ, Schalch T. Capturing structural heterogeneity in chromatin fibers. *J Mol Biol* 2017;429:3031–42. https://doi.org/10.1016/j.jmb.2017.09.002
37. Garcia-Saez I, Menoni H, Boopathi R *et al.* Structure of an H1-Bound 6-Nucleosome array reveals an untwisted two-start chromatin fiber conformation. *Mol Cell* 2018;72:902–15. https://doi.org/10.1016/j.molcel.2018.09.027
38. Song F, Chen P, Sun D *et al.* Cryo-EM study of the chromatin fiber reveals a double helix twisted by tetranucleosomal units. *Science* 2014;344:376–80. https://doi.org/10.1126/science.1251413
39. Woods DC, Rodríguez-Ropero F, Wereszczynski J. The dynamic influence of linker histone saturation within the poly-nucleosome array. *J Mol Biol* 2021;433:166902. https://doi.org/10.1016/j.jmb.2021.166902
40. Portillo-Ledesma S, Schlick T. Bridging chromatin structure and function over a range of experimental spatial and temporal scales by molecular modeling. *WIREs Comput Mol Sci* 2020;10:e1434. https://doi.org/10.1002/wcms.1434
41. Bascom GD, Schlick T. Mesoscale modeling of chromatin fibers. In: Lavelle C, Victor J-M, (eds.), *Nuclear Architecture and Dynamics*. Boston: Academic Press, 2017, 2, 123–47.
42. Li Z, Portillo-Ledesma S, Janani M *et al.* The influence of 10*n* and 10*n*+5 linker lengths on chromatin fiber topologies explored by mesoscale modeling. *Biophys J* 2026;125:1–16. https://doi.org/10.1016/j.bpj.2025.08.030
43. Berman HM, Westbrook J, Feng Z *et al.* The protein data bank. *Nucleic Acids Res* 2000;28:235–42. https://doi.org/10.1093/nar/28.1.235
44. Lin X, Zhang B. Explicit ion modeling predicts physicochemical interactions for chromatin organization. *eLife* 2024;12:RP90073. https://doi.org/10.7554/eLife.90073
45. Zhang M, Díaz-Celis C, Liu J *et al.* Angle between DNA linker and nucleosome core particle regulates array compaction revealed by individual-particle Cryo-electron tomography. *Nat Comm* 2024;15:4395. https://doi.org/10.1038/s41467-024-48305-1
46. Zhang Q, Beard DA, Schlick T. Constructing irregular surfaces to enclose macromolecular complexes for mesoscale modeling using the discrete surface charge optimization (DiSCO) algorithm. *J Comput Chem* 2003;24:2063–74. https://doi.org/10.1002/jcc.10337
47. Beard DA, Schlick T. Modeling salt-mediated electrostatics of macromolecules: the discrete surface charge optimization algorithm and its application to the nucleosome. *Biopolymers* 2001;58:106–15.
48. Jian H, Vologodskii AV, Schlick T. A combined wormlike-chain and bead model for dynamic simulations of long linear DNA. *J Comput Phys* 1997;136:168–79. https://doi.org/10.1006/jcph.1997.5765
49. Arya G, Zhang Q, Schlick T. Flexible histone tails in a new mesoscopic oligonucleosome model. *Biophys J* 2006;91:133–50. https://doi.org/10.1529/biophysj.106.083006
50. Arya G, Schlick T. A tale of tails: how histone tails mediate chromatin compaction in different salt and linker histone environments. *J Phys Chem A* 2009;113:4045–59. https://doi.org/10.1021/jp810375d
51. Luque A, Collepardo-Guevara R, Grigoryev S *et al.* Dynamic condensation of linker histone C-terminal domain regulates chromatin structure. *Nucleic Acids Res* 2014;42:7553–60. https://doi.org/10.1093/nar/gku491
52. Luger K, Mäder AW, Richmond RK *et al.* Crystal structure of the nucleosome core particle at 2.8 Å resolution. *Nature* 1997;389:251–60. https://doi.org/10.1038/38444
53. Hagerman PJ. Flexibility of DNA. *Annu Rev Biophys* 1988;17:265–86. https://doi.org/10.1146/annurev.bb.17.060188.001405
54. Horowitz DS, Wang JC. Torsional rigidity of DNA and length dependence of the free energy of DNA supercoiling. *J Mol Biol* 1984;173:75–91. https://doi.org/10.1016/0022-2836(84)90404-2
55. Drew HR, Travers AA. DNA bending and its relation to nucleosome positioning. *J Mol Biol* 1985;186:773–90. https://doi.org/10.1016/0022-2836(85)90396-1
56. Arya G, Schlick T. Efficient global biopolymer sampling with end-transfer configurational bias Monte Carlo. *J Chem Phys* 2007;126:44107. https://doi.org/10.1063/1.2428305
57. Metropolis N, Ulam S. The Monte Carlo method. *J Am Stat Assoc* 1949;44:335–41. https://doi.org/10.1080/01621459.1949.10483310
58. Lu X-J. DSSR-enabled innovative schematics of 3D nucleic acid structures with PyMOL. *Nucleic Acids Res* 2020;48:e74. https://doi.org/10.1093/nar/gkaa426
59. Li Z, Sun R, Bishop TC. Genome Dashboards: framework and examples. *Biophys J* 2020;118:2077–85. https://doi.org/10.1016/j.bpj.2020.02.018
60. Lu X-J, Olson WK. 3DNA: a software package for the analysis, rebuilding and visualization of three-dimensional nucleic acid structures.. *Nucleic Acids Res* 2003;31:5108–21. https://doi.org/10.1093/nar/gkg680
61. Perišić O, Collepardo-Guevara R, Schlick T. Modeling studies of chromatin fiber structure as a function of DNA linker length. *J Mol Biol* 2010;403:777–802. https://doi.org/10.1016/j.jmb.2010.07.057
62. Collepardo-Guevara R, Schlick T. Chromatin fiber polymorphism triggered by variations of DNA linker lengths. *Proc Natl Acad Sci USA* 2014;111:8061–6. https://doi.org/10.1073/pnas.1315872111
63. Bascom GD, Kim T, Schlick T. Kilobase pair chromatin fiber contacts promoted by living-system-like DNA linker length distributions and nucleosome depletion. *J Phys Chem B* 2017;121:3882–94. https://doi.org/10.1021/acs.jpcb.7b00998

64. McGhee JD, Nickol JM, Felsenfeld G *et al.* Higher order structure of chromatin: orientation of nucleosomes within the 30 nm chromatin solenoid is independent of species and spacer length. *Cell* 1983;33:831–41. https://doi.org/10.1016/0092-8674(83)90025-9
65. Widom J, Klug A. Structure of the 300A chromatin filament: x-ray diffraction from oriented samples. *Cell* 1985;43:207–13. https://doi.org/10.1016/0092-8674(85)90025-x
66. Bednar J, Horowitz RA, Grigoryev SA *et al.* Nucleosomes, linker DNA, and linker histone form a unique structural motif that directs the higher-order folding and compaction of chromatin. *Proc Natl Acad Sci USA* 1998;95:14173–8. https://doi.org/10.1073/pnas.95.24.14173
67. Valouev A, Johnson SM, Boyd SD *et al.* Determinants of nucleosome organization in primary human cells.. *Nature* 2011;474:516–20. https://doi.org/10.1038/nature10002
68. Clarkson C, Deeks E, Samarista R *et al.* CTCF-dependent chromatin boundaries formed by asymmetric nucleosome arrays with decreased linker length. *Nucleic Acids Res* 2019;47:11181–96. https://doi.org/10.1093/nar/gkz908
69. Thorn G, Clarkson C, Rademacher A *et al.* DNA sequence-dependent formation of heterochromatin nanodomains. *Nat Commun* 2022;13:1861. https://doi.org/10.1038/s41467-022-29360-y
70. Todolli S, Nizovtseva EV, Clauvelin N *et al.* Geometric variations in nucleosomal DNA dictate higher-order chromatin structure and enhancer–promoter communication. *J Chem Phys* 2024;161:24510. https://doi.org/10.1063/5.0240991
71. Todolli S, Young RT, Watkins AS *et al.* Surprising twists in nucleosomal DNA with implication for higher-order folding. *J Mol Biol* 2021;433:167121. https://doi.org/10.1016/j.jmb.2021.167121
72. Todolli S, Perez PJ, Clauvelin N *et al.* Contributions of sequence to the higher-order structures of DNA. *Biophys J* 2017;112:416–26. https://doi.org/10.1016/j.bpj.2016.11.017
73. Kenzaki H, Takada S. Linker DNA length is a key to tri-nucleosome folding. *J Mol Biol* 2021;433:166792. https://doi.org/10.1016/j.jmb.2020.166792
74. Brouwer T, Pham C, Kaczmarczyk A *et al.* A critical role for linker DNA in higher-order folding of chromatin fibers. *Nucleic Acids Res* 2021;49:2537–51. https://doi.org/10.1093/nar/gkab058
75. Correll SJ, Schubert MH, Grigoryev SA. Short nucleosome repeats impose rotational modulations on chromatin fibre folding. *EMBO J* 2012;31:2416–26. https://doi.org/10.1038/emboj.2012.80
76. Norouzi D, Katebi A, Cui F *et al.* Topological diversity of chromatin fibers: interplay between nucleosome repeat length, DNA linking number and the level of transcription. *AIMS Biophys* 2015;2:613–29. https://doi.org/10.3934/biophy.2015.4.613
77. Nikitina T, Norouzi D, Grigoryev SA *et al.* DNA topology in chromatin is defined by nucleosome spacing. *Sci Adv* 2017;3:e1700957. https://doi.org/10.1126/sciadv.1700957
78. Bass MV, Nikitina T, Norouzi D *et al.* Nucleosome spacing periodically modulates nucleosome chain folding and DNA topology in circular nucleosome arrays. *J Biol Chem* 2019;294:4233–46. https://doi.org/10.1074/jbc.RA118.006412
79. Portillo-Ledesma S, Wagley M, Schlick T. Chromatin transitions triggered by LH density as epigenetic regulators of the genome. *Nucleic Acids Res* 2022;50:10328–42. https://doi.org/10.1093/nar/gkac757
80. Zhou B-R, Feng H, Huang F *et al.* Structural insights into the cooperative nucleosome recognition and chromatin opening by FOXA1 and GATA4. *Mol Cell* 2024;84:3061–79. https://doi.org/10.1016/j.molcel.2024.07.016
81. Moraru M, Schalch T. Chromatin fiber structural motifs as regulatory hubs of genome function?. *Essays Biochem* 2019;63:123–32. https://doi.org/10.1042/EBC20180065
82. Machida S, Takizawa Y, Ishimaru M *et al.* Structural basis of heterochromatin formation by human HP1. *Mol Cell* 2018;69:385–97. https://doi.org/10.1016/j.molcel.2017.12.011
83. Poepsel S, Kasinath V, Nogales E. Cryo-EM structures of PRC2 simultaneously engaged with two functionally distinct nucleosomes. *Nat Struct Mol Biol* 2018;25:154–62. https://doi.org/10.1038/s41594-018-0023-y
84. Alvarado W, Moller J, Ferguson AL *et al.* Tetranucleosome interactions drive chromatin folding. *ACS Central Science* 2021;7:1019–27. https://doi.org/10.1021/acscentsci.1c00085
85. Li W, Chen P, Yu J *et al.* FACT remodels the tetranucleosomal unit of chromatin fibers for gene transcription. *Mol Cell* 2016;64:120–33. https://doi.org/10.1016/j.molcel.2016.08.024
86. Clapier CR, Iwasa J, Cairns BR *et al.* Mechanisms of action and regulation of ATP-dependent chromatin-remodelling complexes. *Nat Rev Mol Cell Biol* 2017;18:407–22. https://doi.org/10.1038/nrm.2017.26
87. Pommier Y, Nussenzweig A, Takeda S *et al.* Human topoisomerases and their roles in genome stability and organization. *Nat Rev Mol Cell Biol* 2022;23:407–27. https://doi.org/10.1038/s41580-022-00452-3
88. Kable B, Portillo-Ledesma S, Popova EY *et al.* Compromised two-start zigzag chromatin folding in immature mouse retina cells driven by irregularly spaced nucleosomes with short DNA linkers. *Nucleic Acids Res* 2025;53:gkaf457. https://doi.org/10.1093/nar/gkaf457
89. Farr SE, Woods EJ, Joseph JA *et al.* Nucleosome plasticity is a critical element of chromatin liquid–liquid phase separation and multivalent nucleosome interactions. *Nat Comm* 2021;12:2883. https://doi.org/10.1038/s41467-021-23090-3
90. Hou Z, Nightingale F, Zhu Y *et al.* Structure of native chromatin fibres revealed by Cryo-ET *in situ*. *Nat Comm* 2023;14:6324. https://doi.org/10.1038/s41467-023-42072-1
91. Rowley MJ, Corces VG. Organizational principles of 3D genome architecture. *Nat Rev Genet* 2018;19:789–800. https://doi.org/10.1038/s41576-018-0060-8
92. Bajpai G, Jain I, Inamdar MM *et al.* Binding of DNA-bending non-histone proteins destabilizes regular 30-nm chromatin structure. *PLOS Comput Biol* 2017;13:1–19. https://doi.org/10.1371/journal.pcbi.1005365
93. Liu S, Lin X, Zhang B. Chromatin fiber breaks into clutches under tension and crowding. *Nucleic Acids Res* 2022;50:9738–47. https://doi.org/10.1093/nar/gkac725
94. Oh I, Choi S, Jung Y *et al.* Entropic effect of macromolecular crowding enhances binding between nucleosome clutches in heterochromatin, but not in euchromatin. *Sci Rep* 2018;8:5469. https://doi.org/10.1038/s41598-018-23753-0
95. Depken M, Schiessel H. Nucleosome shape dictates chromatin fiber structure. *Biophys J* 2009;96:777–84. https://doi.org/10.1016/j.bpj.2008.09.055
96. Müller O, Kepper N, Schöpflin R *et al.* Changing chromatin fiber conformation by nucleosome repositioning. *Biophys J* 2014;107:2141–50. https://doi.org/10.1016/j.bpj.2014.09.026
97. Perišić O, Portillo-Ledesma S, Schlick T. Sensitive effect of linker histone binding mode and subtype on chromatin condensation. *Nucleic Acids Res* 2019;47:4948–57. https://doi.org/10.1093/nar/gkz234
98. Collepardo-Guevara R, Schlick T. Crucial role of dynamic linker histone binding and divalent ions for DNA accessibility and gene regulation revealed by mesoscale modeling of oligonucleosomes. *Nucleic Acids Res* 2012;40:8803–17. https://doi.org/10.1093/nar/gks600
99. Collepardo-Guevara R, Schlick T. The effect of linker histone's nucleosome binding affinity on chromatin unfolding mechanisms. *Biophys J* 2011;101:1670–80. https://doi.org/10.1016/j.bpj.2011.07.044
100. Grigoryev SA, Bascom G, Buckwalter JM *et al.* Hierarchical looping of zigzag nucleosome chains in metaphase chromosomes.

Proc Natl Acad Sci USA 2016;113:1238–43. https://doi.org/10.1073/pnas.1518280113
101. Luque A, Ozer G, Schlick T. Correlation among DNA linker length, linker histone concentration, and histone tails in chromatin. *Biophys J* 2016;110:2309–19. https://doi.org/10.1016/j.bpj.2016.04.024
102. Bascom GD, Schlick T. Chromatin fiber folding directed by cooperative histone tail acetylation and linker histone binding. *Biophys J* 2018;114:2376–85. https://doi.org/10.1016/j.bpj.2018.03.008
103. Portillo-Ledesma S, Chung S, Hoffman J *et al.* Regulation of chromatin architecture by transcription factor binding. *eLife* 2024;12:RP91320. https://doi.org/10.7554/eLife.91320
104. Bascom GD, Sanbonmatsu KY, Schlick T. Mesoscale modeling reveals hierarchical looping of chromatin fibers near gene regulatory elements. *J Phys Chem B* 2016;120:8642–53. https://doi.org/10.1021/acs.jpcb.6b03197
105. Bascom GD, Myers CG, Schlick T. Mesoscale modeling reveals formation of an epigenetically driven HOXC gene hub. *Proc Natl Acad Sci USA* 2019;116:4955–62. https://doi.org/10.1073/pnas.1816424116
106. Portillo-Ledesma S, Hang M, Schlick T. Regulation of genome architecture in huntington's disease. *Biochem* 2025;64:2100–15. https://doi.org/10.1021/acs.biochem.5c00029
107. Kadam S, Schlick T. Multiscale chromatin modeling of chromosome X structural changes upon inactivation highlights the differential regulatory mechanism of Xist. bioRxiv, https://doi.org/10.64898/2026.01.20.700676, 20 January 2026, preprint: not peer reviewed.
108. Kreysing JP, Cruz-León S, Betz J *et al.* Molecular architecture of heterochromatin at the nuclear periphery of primary human cells. *Nat Commun* 2026;17:5844. https://doi.org/10.1038/s41467-026-75087-5
109. Zhou H, Huertas J, Maristany MJ *et al.* Multiscale structure of chromatin condensates explains phase separation and material properties. *Science* 2025;390:eadv6588. https://doi.org/10.1126/science.adv6588
110. Fatmaoui F, Carrivain P, Taiki F *et al.* Direct visualization and tracing of chromatin folding in the Drosophila embryo. *The EMBO J* 2026;45:1621–47. https://doi.org/10.1038/s44318-026-00701-7
111. Haynes KA. Chromatin research and biological engineering: an evolving relationship poised for new biomedical impacts. *Curr Opin Syst Biol* 2019;14:73–81. https://doi.org/10.1016/j.coisb.2019.02.011
112. Kim J, Kim J, Park M. Synthetic interventions in epigenome: unraveling chromatin's potential for therapeutic applications. *Curr Opin Syst Biol* 2024;37:100504. https://doi.org/10.1016/j.coisb.2023.100504

Received: June 25, 2026. **Revised:** September 3, 2026. **Accepted:** September 17, 2026
© The Author(s) 2026. Published by Oxford University Press.
This is an Open Access article distributed under the terms of the Creative Commons Attribution-NonCommercial License (https://creativecommons.org/licenses/by-nc/4.0/), which permits non-commercial re-use, distribution, and reproduction in any medium, provided the original work is properly cited. For commercial re-use, please contact reprints@oup.com for reprints and translation rights for reprints. All other permissions can be obtained through our RightsLink service via the Permissions link on the article page on our site-for further information please contact journals.permissions@oup.com.